AD-A110 079 OHIO STATE UNIV COLUMBUS F/G 20/3
SURFACE CURRENT AND CHARGE DENSITY INDUCED ON AN INFINITE, PERF--ETC(U)
JUN 77 L ERSOY, N WANG
UNCLASSIFIED NOTES-338 NL

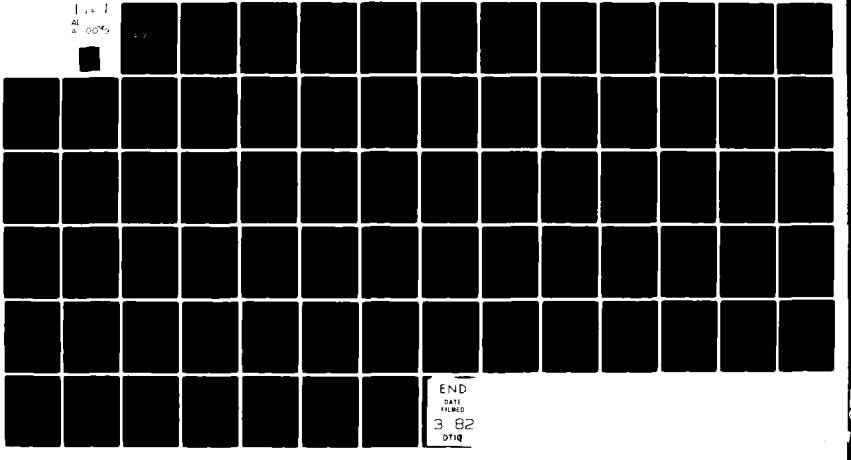

END
DATE FILMED
3 82
DTIC

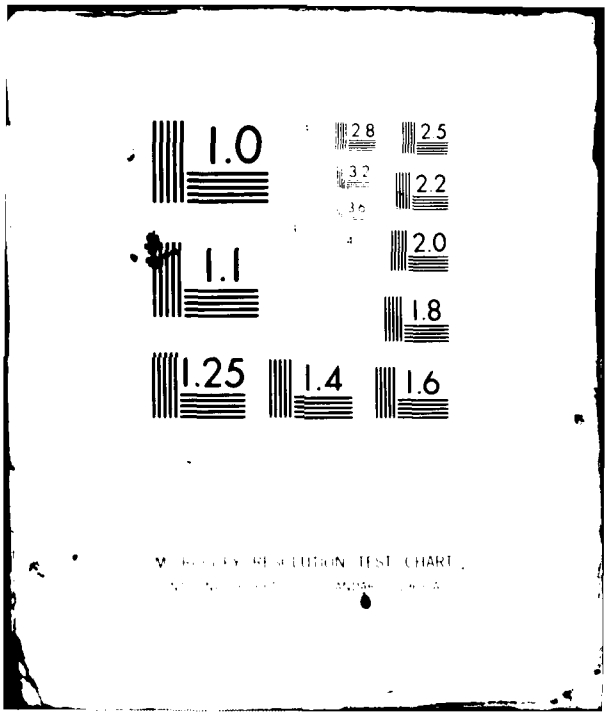
1.0
2.8
2.5
3.2
2.2
3.6
2.0
1.1
1.8
1.25
1.4
1.6

LEVEL 1

Interaction Notes

Note-338

June 1977

Surface Current and Charge Density Induced on an Infinite, Perfectly Conducting Circular Cylinder in the Presence of Finite Axial Thin Wire - Transverse Magnetic Case

L. Ersoy and N. Wang

Ohio State University
Columbus, Ohio

ABSTRACT

The induced surface current and charge densities are evaluated on an infinitely long circular cylinder in the presence of a set of axial wires. The incident field is taken as a TM_z polarized plane wave in the principal plane. The method used for the calculations is a hybrid solution which combines the eigenfunction solution for a circular cylinder (infinitely long) and the reaction integral equation formulation for thin axial wires. In principle, this solution is a modified moment method technique which employs cylindrical Green's functions in order to introduce the effect of the infinitely long circular cylinder into the problem. The fields penetrated by the axial dipoles are also given in terms of the cylindrical Green's functions.

TABLE OF CONTENTS

SECTION I

INTRODUCTION

In this report, the induced surface current and charge densities ($\bar{J}_s, \rho_s$) are evaluated on an infinitely large circular cylinder in the presence of a set of axial wires excited by a plane wave incident in the mid frequency range. One of the reasons for doing this is to introduce a procedure which can eventually be extended to the cases where there are sets of radial and circumferential wires in the presence of an infinitely long circular cylinder in order to model the "detailed structure" of an aircraft between the frequencies 20 and 50 MHz (the mid-frequency range). The surface current and charge densities mentioned above, may be induced by lightning or by the electromagnetic pulse (EMP) and their evaluation would be of value to designers for the prevention of damage caused by such phenomena. These quantities, by reciprocity, also represent the Green's function for the aircraft, and accordingly the performance of an antenna placed on the vehicle can be evaluated by use of these "aircraft" Green's functions.

Previous computations have given both the surface current and charge densities for the low frequency region where moment method solutions are applicable (below 10 MHz for a B-1 aircraft) [1,2] and the high frequency range where Geometrical Theory of Diffraction (GTD) techniques are appropriate (above 50 MHz for a B-1 aircraft) [3,4].

Richmond [5] developed one of the first moment method solutions for aircraft structures. These solutions required approximately 100 unknown currents per square wavelength [5,6,7]. A later method, a surface-current approach, reduced the unknown currents to about 20 per square wavelength [8]. Lin [9] pointed out that continuously conducting surfaces can be closely simulated by a wire grid structure when the dimensions of the mesh apertures are about $\lambda/10$. Richmond [10] indicated that 2λ is the maximum length for an aircraft to be handled by the moment method technique. Scattering cross section calculations for aircraft less than 0.8λ in length are found to be within 10 percent of measured data [11]. The reasons for these restrictions are due to the limitation on the size of matrices which modern computers can solve without excessive loss of accuracy and computation time [12].

In recent years, Burnside et al. successfully applied GTD techniques to aircraft scattering problems [13,14,15,16,17]. This technique is most useful when distances between the scattering centers are greater than approximately $\lambda/2$. Even for those cases where this requirement can be relaxed, GTD techniques are restricted to high frequencies. The low frequency limit is around 100 MHz. The upper frequency limit is dependent on how well the theoretical model simulates the important details of the actual structure. A formal presentation of GTD can be found in the works of Keller [18] and Kouyoumjian et al. [19,20,21].

The present approach is intended to partially fill the gap between moment method solutions and the GTD techniques. In this frequency range the wings are too narrow to be represented by a GTD solution and the aircraft has too long a surface area to be handled by the moment method approach. These restrictions preclude treatment of aircraft geometries where the length resonances are dominant.

In general, an aircraft can be modeled as an infinitely long cylinder (representing the fuselage) and an array of thin wires (representing the wings). As a first step toward such an aircraft model, in this work, a set of axial thin wires in the presence of a cylinder is analyzed. Actually, the technique presented here can be extended to any structure which can be represented by an infinitely long circular cylinder in the presence of additional scatterers which can be modeled as wire-grid structures. The only requirement is that the additional scatterers must be small enough so that they can be included by themselves in a momemt method technique. A general aircraft model is shown in Figure 1.

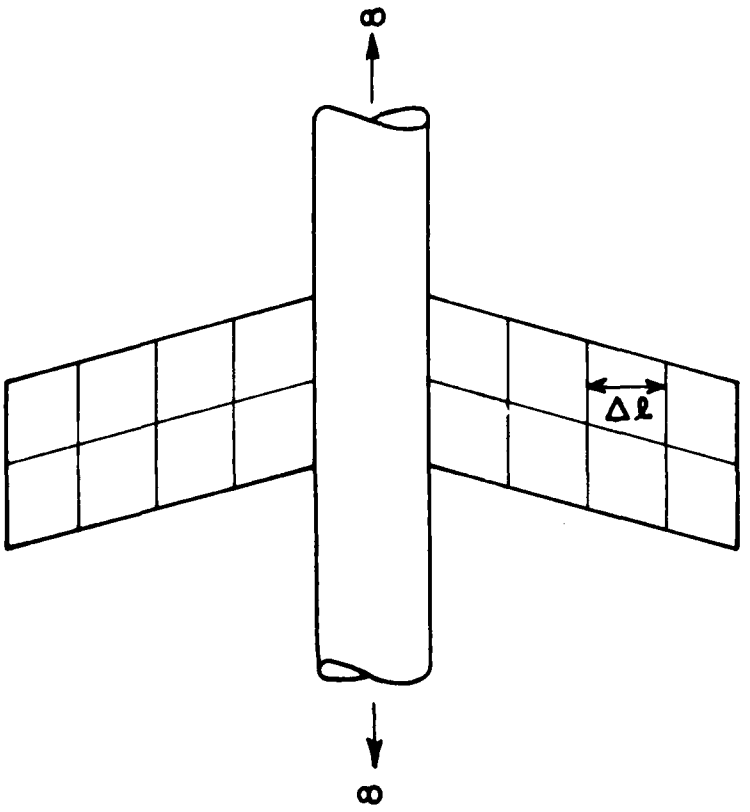

Figure 1 A typical aircraft structure.

Additional scatterers are modeled by a set of axial wires in order to set up a moment method solution. However their associated fields are expanded in terms of the cylindrical functions so that these will in turn satisfy the boundary conditions over the surface of the cylinder which represents the fuselage.

Throughout this paper, the medium of the scatterer is taken to be free space.

An incident plane wave is described by the incident angles (θ_i,ϕ_i). The wings are assumed to be flat, i.e., the wires modeling the wings are taken as the $\hat{z}$ and $\hat{\rho}$ oriented segments. The cylindrical coordinate system used for the calculations is presented in Figure 6, Section III.

The induced surface current and charge densities $(\overline{J}_s,\rho_s)$ on the surface of the cylinder can be described by

$$\overline{J}_s = \overline{J}_s^o + \Delta\overline{J}_s \tag{1-a}$$

$$\rho_s = \rho_s^o + \Delta\rho_s \tag{1-b}$$

$(\overline{J}_s^o,\rho_s^o)$ are generated on the cylinder without wings by the incident plane wave. They can be calculated by expending the incident plane wave fields in terms of the cylindrical Bessel functions and enforcing the boundary conditions on the fuselage. In this manner the field $(\overline{E}^o,\overline{H}^o)$ can be obtained on the surface of the cylinder. Then the induced surface current density, $\overline{J}_s^o$, is given by

$$\overline{J}_s^o = \hat{n} \times \overline{H}^o \tag{2}$$

and the charge density

$$\rho_s^o = \varepsilon_o \hat{n} \cdot \overline{E}^o \tag{3}$$

where $\hat{n}$ is the outward directed normal vector on the fuselage.

$\Delta\overline{J}_s$ and $\Delta\rho_s$ are the current and charge densities induced on the cylinder by currents that flow on the wire segments representing the aircraft wings (in the presence of the fuselage). Consider, for example, the m^{th} segment. A current $I_m(\overline{r}')$ is induced on that segment. In turn, $I_m(\overline{r}')$ generates a field $(\overline{E}_m,\overline{H}_m)$ which can be written as

$$\overline{E}^m(\overline{r}) = \int \tilde{\overline{E}}(\overline{r}|\overline{r}') \cdot I_m(\overline{r}')d\overline{r}' \tag{4}$$

where $E(\bar{r}\ \bar{r}')$ is the dyadic electric field at a point $\bar{r}$ of an infinitesimal dipole of unit magnitude located at $\bar{r}'$ in the presence of the cylinder. Again, I_m is the current magnitude on the m^{th} wire and these are found from the moment method solution. The magnetic field is also found similarly. Fields at the surface of the cylinder, from these current elements, can now be used to find the induced surface current and charge densities as follows:

$$\Delta\bar{J}_m = \hat{n} \times H^m(a,z,\phi) \tag{5}$$

and

$$\Delta\rho_m = \varepsilon_o\, \hat{n} \cdot \bar{E}^m(a,z,\phi) \tag{6}$$

where a denotes the radials of the cylinder. The total current and charge densities are found from superposition theorem as

$$\bar{J}_s = \bar{J}_s^o + \sum_{m=1}^{N} \Delta\bar{J}_m \tag{7}$$

and

$$\rho_s = \rho_s^o + \sum_{m=1}^{N} \Delta\rho_m \tag{8}$$

so that

$$\Delta\bar{J}_s = \sum_{m=1}^{N} \Delta\bar{J}_m \tag{9}$$

and

$$\Delta\rho_s = \sum_{m=1}^{N} \Delta\rho_m \tag{10}$$

and N is the total number of wire segments used to model the scatterers.

Equations (7) and (8) give $\bar{J}_s$ and ρ_s over the surface of the cylinder. The currents on the surface of the wings have already been evaluated and are given by the value of I_m at each point. The surface current density is simply $I_m/\Delta\ell$ where $\Delta\ell$ is now the width of a cell or

wire spacing as seen in Figure 1 (flat plate model). The surface charge density here would be obtained from the equation of continuity

$$\overline{\rho}_s = -\frac{1}{j\omega} \nabla \cdot \overline{J}_s \tag{11}$$

where $j = \sqrt{-1}$. Throughout this paper, $e^{j\omega t}$ time conversion is understood and suppressed.

In the following paragraphs, a detailed treatment of the hybrid moment method is introduced. The moment method technique is also included in this paper for completeness and to establish the ties between the previous work and the hybrid technique. The version of the moment method presented in the following sections is the one developed and used to produce the results in this paper. A number of papers have been written on this subject, and a more detailed treatment of this method can be found throughout the literature [22].

SECTION II

THE MOMENT METHOD SOLUTION OBTAINED FROM THE REACTION INTEGRAL EQUATION

Consider the reciprocity theorem in the following form

$$\int (\bar{E}_a \cdot \bar{J}_b - \bar{H}_a \cdot \bar{M}_b) d\bar{r} = \int (\bar{E}_b \cdot \bar{J}_a - \bar{H}_b \cdot \bar{M}_a) d\bar{r} \tag{12}$$

where the fields $(\bar{E}_a, \bar{H}_a)$ and $(\bar{E}_b, \bar{H}_b)$ are generated by the sources $(\bar{J}_a, \bar{M}_a)$ and $(\bar{J}_b, \bar{M}_b)$ respectively [23]. As indicated earlier the medium of the scatterer and the sources is taken to be free space.

The field quantities are related to the sources by the following equations

$$\bar{E}_i(\bar{r}) = -j\omega\mu_o \int_{\text{all space}} \tilde{\bar{G}}_e(\bar{r}|\bar{r}') \cdot \bar{J}_i(\bar{r}') d\bar{r}' \tag{13}$$

and

$$\bar{H}_i(\bar{r}) = -j\omega\varepsilon_o \int_{\text{all space}} \tilde{\bar{G}}_m(\bar{r}|\bar{r}') \cdot \bar{M}_i(\bar{r}') d\bar{r}' \tag{14}$$

$\tilde{\bar{G}}_e(\bar{r}|\bar{r}')$ and $\tilde{\bar{G}}_m(\bar{r}|\bar{r}')$ are the electric and magnetic dyadic Green's functions, respectively.

Now, assume there is an external source $(\bar{J}_i, \bar{M}_i)$ generating the field $(\bar{E}, \bar{H})$ in the presence of a closed surface, S (see Figure 2).

The reciprocity equation between the source $(\bar{J}_i, \bar{M}_i)$ and a test source $(\bar{J}_t, \bar{M}_t)$ which is placed inside the closed surface is given as

$$\int (\bar{E} \cdot \bar{J}_t - H \cdot \bar{M}_t) dv = \int (\bar{E}_t \cdot \bar{J}_i - \bar{H}_t \cdot \bar{M}_i) dv \tag{15}$$

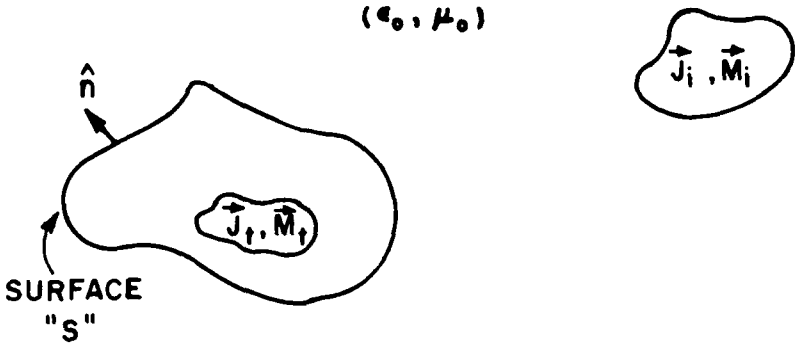

Figure 2. Schematic representation of sources.

where $(\overline{E}_t,\overline{H}_t)$ are the fields generated by the test source $(\overline{J}_t,\overline{M}_t)$ in free space.

If the surface, S, is conductive then the field inside the closed surface is zero.

When the integrals in Equation (15) are restricted to the internal region of the surface, S, then Equation (15) reduces to

$$\int_{\substack{\text{interior of} \\ S}} (\overline{E}_t \cdot \overline{J}_i - \overline{H}_t \cdot \overline{M}_i) dv = 0 \tag{16}$$

and

$$\int_{\substack{\text{interior of} \\ S}} (\overline{E} \cdot \overline{J}_t - \overline{H} \cdot \overline{M}_t) dv = 0 \tag{17}$$

since the fields $(\overline{E},\overline{H})$ vanish inside the conducting media [24].

The incident field $(\overline{E}_i,\overline{H}_i)$ is defined as the field generated by the external source $(\overline{J}_i,\overline{M}_i)$ without the scatterer, S. Then the scattered field $(\overline{E}_s,\overline{H}_s)$ is defined as follows:

$$\overline{E}_s = \overline{E} - \overline{E}_i \tag{18a}$$

$$\overline{H}_s = \overline{H} - \overline{H}_i \tag{18b}$$

Substituting Equations (18a,b) into Equation (17) results in

$$\int_{\substack{\text{interior of}\\ S}} (\bar{E}_s \cdot \bar{J}_t - \bar{H}_s \cdot \bar{M}_t) dv = - \int_{\substack{\text{interior of}\\ S}} (\bar{E}_i \cdot \bar{J}_t - \bar{H}_i \cdot \bar{M}_t) dv \tag{19}$$

Equation (15) is one form of reaction integral equation (RIE). Another form of reaction integral equation can be obtained from Equation (19) and reciprocity theorem (Equation (12))

$$\int (\bar{E}_t \cdot \bar{J}_s - \bar{H}_t \cdot \bar{M}_s) dv = - \int (\bar{E}_t \cdot \bar{J}_i - \bar{H}_t \cdot \bar{M}_i) dv \tag{20}$$

where $(\bar{J}_s, \bar{M}_s)$ are the surface current densities which generate the scattered field $(\bar{E}_s, \bar{H}_s)$ and are defined as follows:

$$\bar{J}_s = \hat{n} \times \bar{H} \tag{21}$$

$$\bar{M}_s = \bar{E} \times \hat{n} \tag{22}$$

On a perfectly conductive surface, the magnetic current density vanishes. Then Equation (20) takes the following form:

$$\int (\bar{E}_t \cdot \bar{J}_i - \bar{H}_t \cdot \bar{M}_i) dv = - \int \bar{E}_t \cdot \bar{J}_s \, dv \tag{23}$$

For a given field $(\bar{E}_t, \bar{H}_t)$, Equation (23) represents an integral equation with J_s as the unknown. One way to solve such an equation is to expand the unknown function in a given set of basis functions

$$\bar{J}_s = \sum_n I_n \bar{F}_n \tag{24}$$

where I_n are the unknown complex coefficients and F_n are the basis functions of our choice.

Substituting Equation (24) into Equation (23), one obtains

$$\int(\bar{E}_t\cdot\bar{J}_i - \bar{H}_t\cdot\bar{M}_i)d\bar{r} = -\sum_n I_n \int \bar{E}_t \cdot \bar{F}_n \, d\bar{r} \tag{25}$$

Equation (25) is one equation with n unknowns: $I_1, I_2, \cdots I_n$. In order to obtain n such equations, the test source (J_t,M_t) can be moved to n different places inside the scattered body. Denoting (E_t^m,H_t^m) as the fields generated by the test source $(\bar{J}_t,\bar{M}_t)$ when it is located at the position m

$$\int(\bar{E}_t^m\cdot\bar{J}_i - \bar{H}_t^m\cdot\bar{M}_i)d\bar{r} = -\sum_n I_n \int \bar{E}_t^m\cdot\bar{F}_n \, d\bar{r} \quad m=1,2,\cdots n \tag{26}$$

Equation (26) defines n linearly independent equations with n unknowns and can simply be written as

$$v_m = \sum_n I_n Z_{mn} \quad m=1,2,\cdots n \tag{27}$$

or in matrix rotation

$$(v) = (I)[Z] \tag{28}$$

where

$$v_m = \int(E_t^m\cdot\bar{J}_i - \bar{H}_t^m\cdot\bar{M}_i)d\bar{r} \tag{29}$$

and

$$z_{mn} = -\int \bar{E}_t^m \cdot \bar{F}_n \, d\bar{r} \tag{30}$$

The unknown currents I_n can be solved by simply inverting the [Z] matrix and multiplying by (V)

$$(I) = (V)\,[Z]^{-1} \tag{31}$$

Employing the reciprocity theorem one more time, Equation (29) can be expressed in a slightly more useful form

$$v_m = \int (\bar{E}_i \cdot \bar{J}_t^m - \bar{H}_i \cdot \bar{M}_t^m) d\bar{r} \tag{32}$$

where $(\bar{J}_t^m, \bar{M}_t^m)$ denotes the test source $(\bar{J}_t \cdot \bar{M}_t)$ positioned at location m and as before $(\bar{E}_i, \bar{H}_i)$ is the incident field.

In Galerkin's formulation of the moment method, the test source $(\bar{J}_t, \bar{M}_t)$ is expanded in the same set of basis functions as are the current densities $\bar{J}_s$.

By virtue of Equation (13) with changing the index i to t Equations (30) and (32) can be rewritten as

$$v_m = \int \bar{E}_i \cdot \bar{F}_m \, d\bar{r} \tag{33a}$$

$$z_{mn} = -\int d\bar{r} \int d\bar{r}' \; \bar{F}_n(\bar{r}) \cdot \tilde{\bar{L}}(\bar{r}|\bar{r}') \cdot \bar{F}_m(\bar{r}') \tag{33b}$$

where $\tilde{\bar{L}}(\bar{r}|\bar{r}')$ is defined by the following equation

$$\tilde{\bar{L}}(\bar{r}|\bar{r}') = -j\omega\mu_o \tilde{\bar{G}}_e(\bar{r}|\bar{r}') \tag{34}$$

such that a $\hat{c}$ oriented infinitesimal electric dipole located at point $\bar{r}'$ generates an electric field $\bar{E}(\bar{r}|\bar{r}')$ at point $\bar{r}$ by the following relation

$$\bar{E}(\bar{r}|\bar{r}') = \tilde{\bar{L}}(\bar{r}|\bar{r}') \cdot \hat{c} \tag{35}$$

where $\hat{c}$ is the unit vector.

In the process of deriving Equations (33a,b), it is assumed that the wires are perfectly conductive and therefore there are no magnetic current densities on them. The same assumption is employed throughout this paper.

Equation (31) and Equations (33a,b) constitute the moment method.

SECTION III
HYBRID MOMENT METHOD

The principle behind the hybrid techniques can be outlined as follows:

1. The scatterer is divided into subsections so that each can be handled by one of the standard mathematical methods developed for electromagnetic problems when the rest of the scatterer is absent. In this paper the superscript "o" is used to denote such quantities (for example $\overline{J}_s^o$, ρ_s^o, Z_{mn}^o) and the term "isolated" is placed in front of them in order to indicate that only one of the subsections of the whole scatterer is under consideration (for example isolated mutual impedance). A schematic representation of this situation is shown in Figures 3(a,b).

2. The interaction between the subsectional scatterers is introduced to the problem as a correction term. The notation "Δ" and the term "perturbed" is used with such quantities (for example $\Delta\overline{J}_s$, ΔZ_{mn}, perturbed mutual impedance). This case is illustrated in Figures 4(a,b).

In this paper, the scatterer is divided into two principle parts: An infinitely long circular cylinder, and the rest of the scatterer. Eigensolutions and the moment method techniques are the tools used for calculating the "isolated" and "perturbed" quantities. As indicated earlier, in order to employ moment method techniques, the scatterers, other than the circular cylinder, are modeled as wire grid structures (the term "additional scatterers" is used in order to identify these structures). Figures 5(a,b,c) schematically illustrate some of these "isolated" and "perturbed" quantities and the general geometry.

Superposition theorem is used to obtain the final results such that

$$\overline{J}_s = \overline{J}_s^o + \Delta\overline{J}_s \tag{36a}$$

$$\rho_s = \rho_s^o + \Delta\rho_s \tag{36b}$$

$$Z_{mn} = z_{mn}^o + \Delta Z_{mn} \tag{36c}$$

$$V_m = V_m^o + \Delta V_m \tag{36d}$$

where $m = 1,2,\cdots N$

$n = 1,2,\cdots N$

and N is the total number of segments used to model the additional scatterers.

In the above equations, Z_{mn}^o is the isolated mutual impedance between the dipoles modeling the additional scatterers. ΔZ_{mn} introduces the effect of the cylinder on the impedance. ΔV_m^o is the isolated open circuit voltage at the terminals of the dipoles modeling the additional scatterers due to the direct plane wave incident. V_m denotes the perturbed open circuit voltage as a result of the fields scattered from the cylinders.

The quantities in Equations (36a,b) are described in the previous pages. Precise mathematical expressions for the quantities introduced above are presented in the following sections.

Because of the cylindrical symmetry, cylindrical coordinate system is employed in this paper. The axis of the cylinder is chosen as the z-axis. Figure 6 illustrates this coordinate system. An incident plane wave is described by the incident angles, θ_i and ϕ_i, as shown in Figure 6.

Axial, radial and phi oriented wire segments can be chosen as the three canonical cases for this problem. In Figure 7, these three canonical cases are illustrated.

Axial dipoles are considered here as a first step in developing the analysis for this rather complex solution. It is recognized that this present solution is in itself representative of an aircraft structure with straight wings only for incident waves perpendicular to the cylinder and polarized parallel to the cylinder. For waves polarized perpendicular to the cylinder, the current flow on the wings has a dominant component normal to the axial dipoles which, of course, cannot exist when only the axial dipoles exist. There is also such a significant nonaxial current component for waves that are not normally incident on the cylinder. Further, if there is any diffraction process that yields a nonaxial current component, then the solution presented here is not applicable. For example, this implies that aircraft with swept back wings would require the use of radial dipoles. Research directed toward generated similar solutions for the radial and phi oriented wires is underway but has not yet reached a state such that it can be included in this thesis.

For each canonical problem, the following steps can be taken in order to obtain surface charge and current densities ($\rho_s, \bar{J}_s$) induced on the surface of the cylinder due to a plane wave.

a. Calculate ($\rho_s^o, \bar{J}_s^o$) using an eigenfunction expansion of the incident fields and the boundary conditions.

b. Calculate the current magnitudes on the wire segments which are used to model the aircraft wings by the moment method technique.

c. Determine the fields ($\bar{E}_m, \bar{H}_m$) generated by these current segments and obtain the resulting surface current and charge densities from using these fields.

d. Using the superposition theorem, find the total induced surface charge and current densities at a given point on the surface of the cylinder.

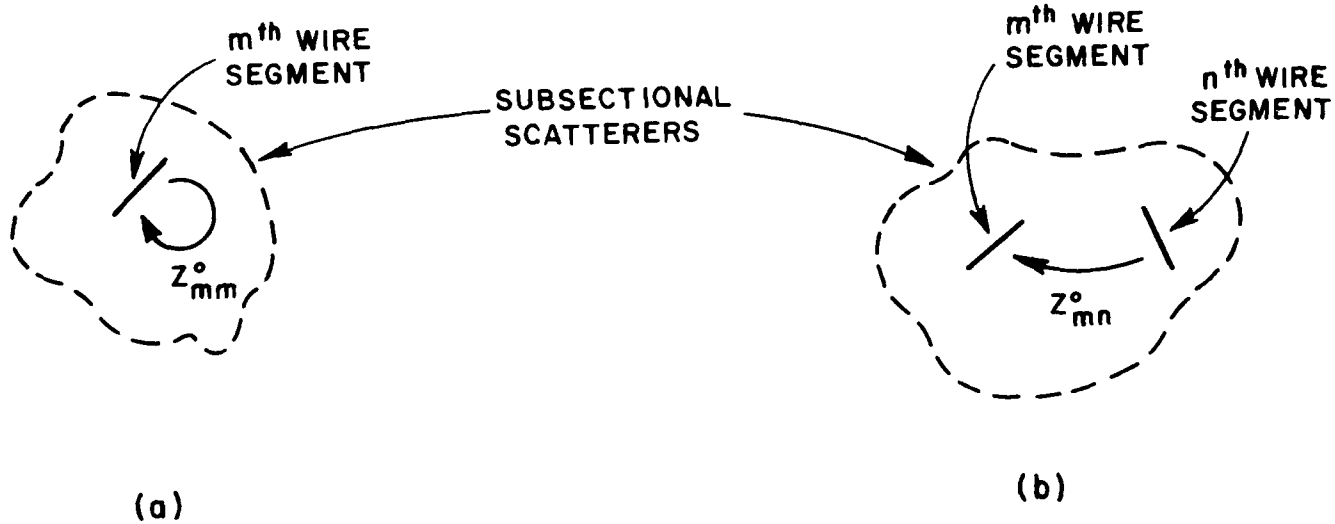

Figure 3. Schematic representatives of isolated (a) self and (b) mutual impedances.

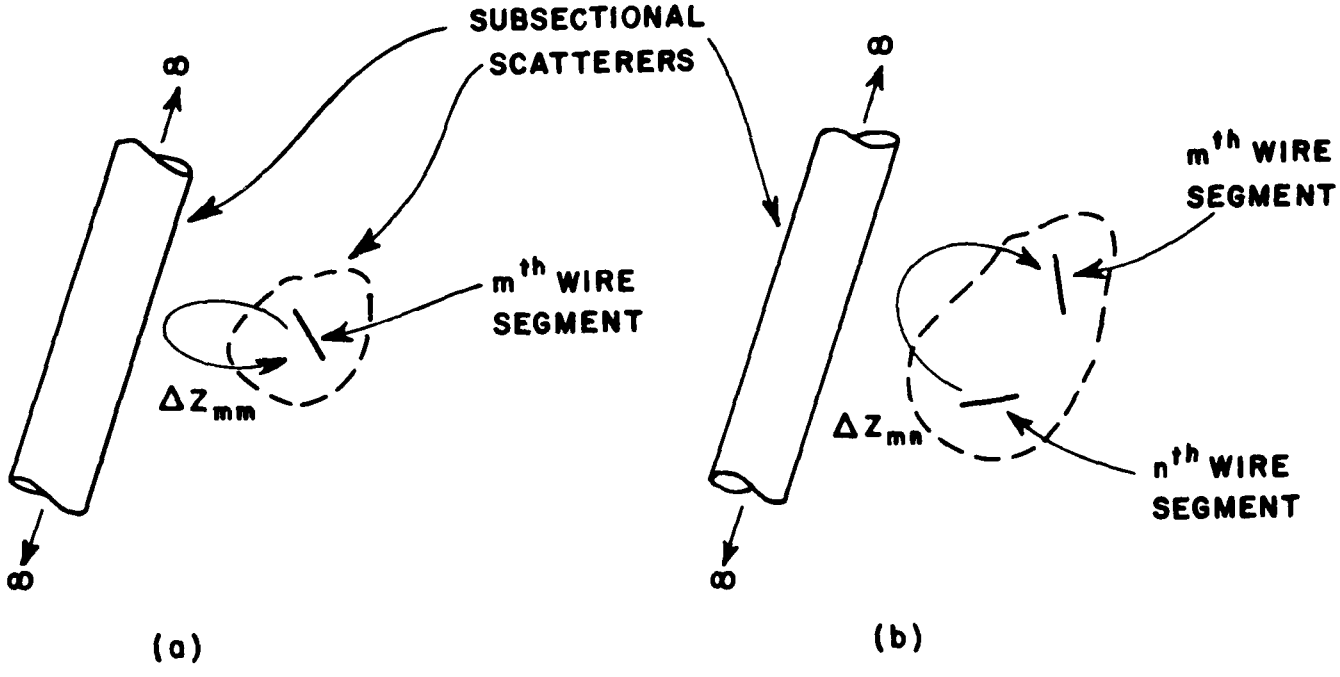

Figure 4. Schematic representatives of perturbed (a) self and (b) mutual impedances.

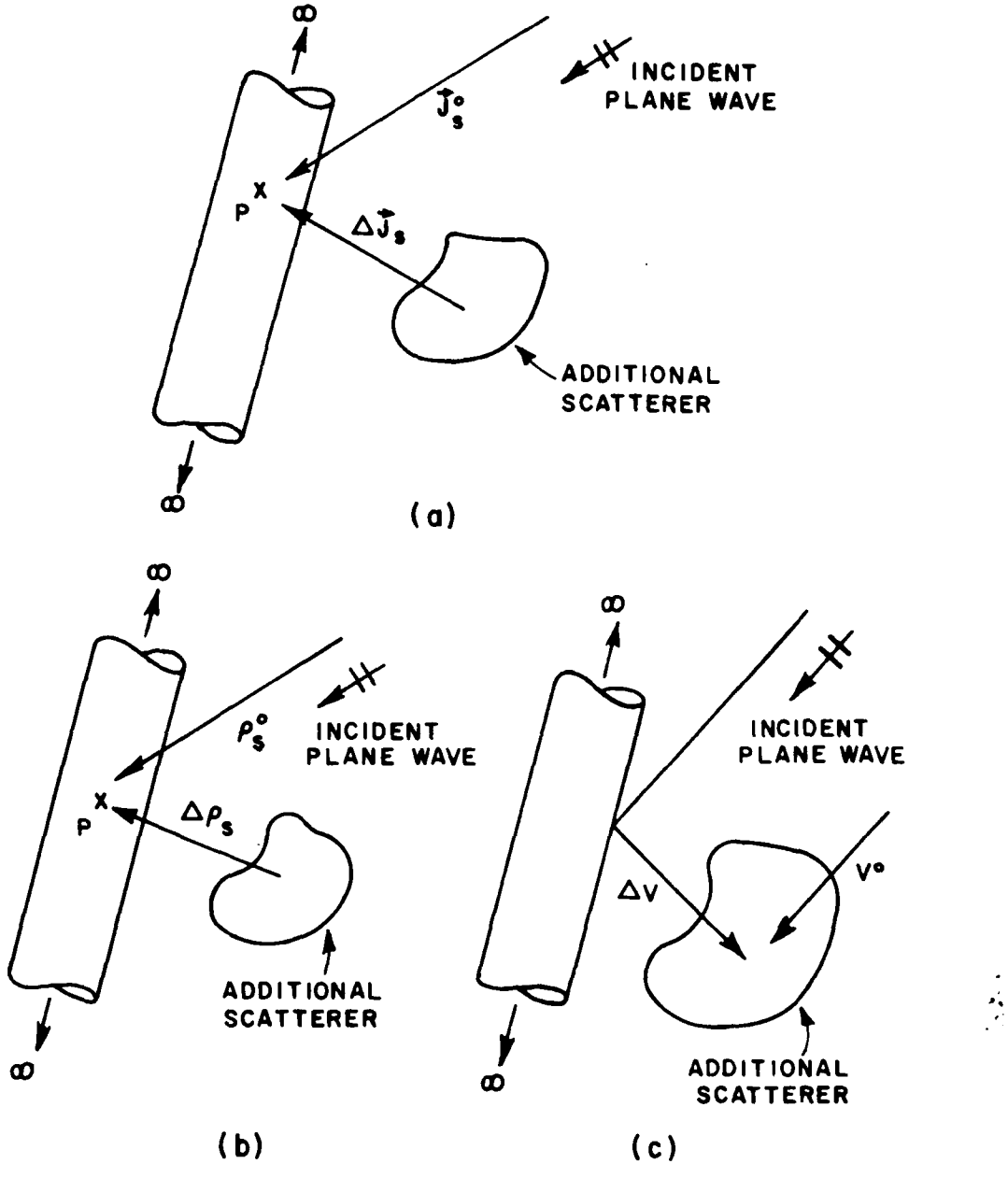

Figure 5. Schematic representatives of some of the "isolated" and "perturbed" quantities.

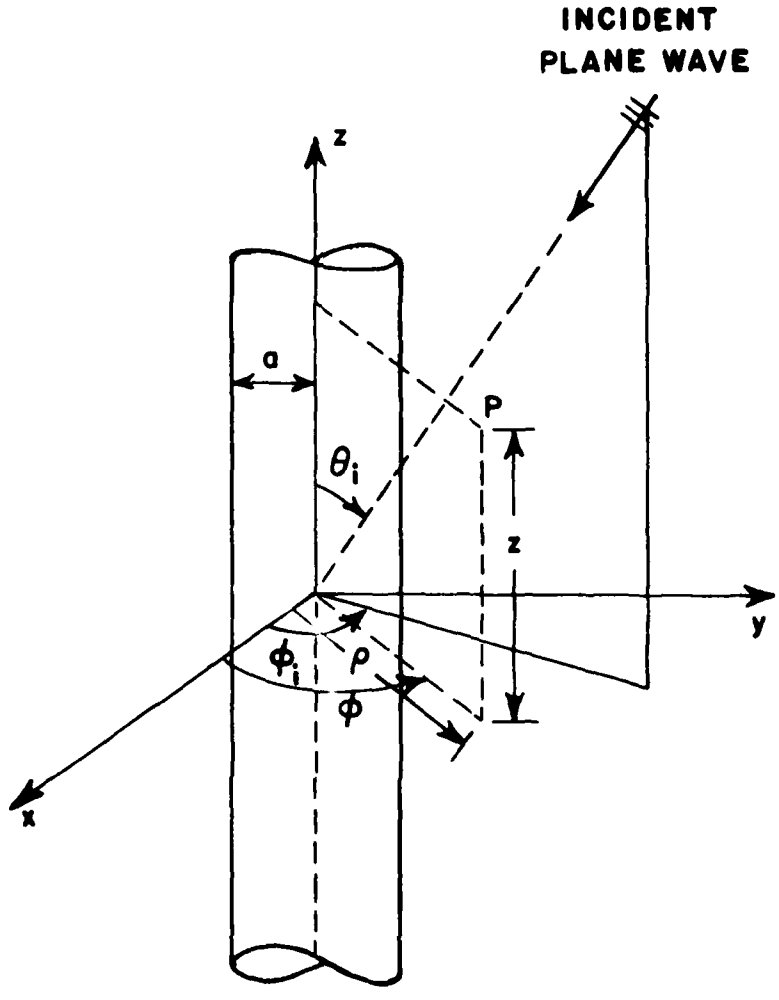

Figure 6. Cylindrical coordinate system.

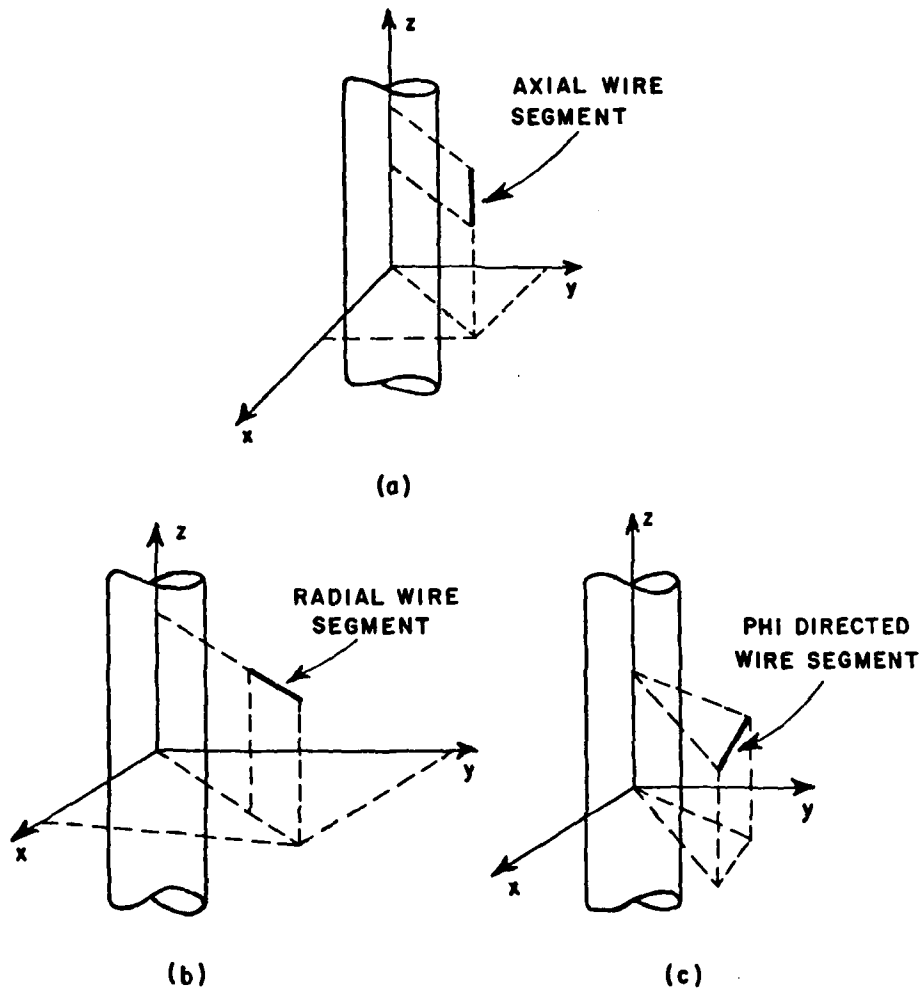

Figure 7. Axial, radial and phi directed dipoles.

SECTION IV
AXIAL DIPOLE

1. Analysis

The procedure introduced in the previous section is employed in the following pages. The geometry used for this chapter is presented in Figure 8. In order to establish a foothold for the future work, the calculations for an arbitrarily incident, TM_z polarized plane wave. The electric field of such a plane wave is given by

$$\overline{E}_i(z,\rho,\phi) = \hat{e}_i \cdot e^{jk(\rho\sin\theta_i\cos(\phi_i-\phi)+z\cos\theta_i)} \tag{37}$$

where the observation point is represented by cylindrical coordinates ρ, z and ϕ. θ_i and ϕ_i describe the incident plane wave and are shown in Figures 6 and 8.

In particular, $\theta_i = 90°$ is the interest of this paper.

a. Calculation of $(\overline{J}_s^o, \rho_s^o)$

Surface current and charge densities, in the absence of the axial dipoles, can be calculated by simply expanding the incident plane wave in cylindrical Bessel functions and enforcing the boundary conditions on the surface of the cylinder.

For the incident field given in Equation (37), the total z component of the electric field is

$$\overline{E}_z = -\hat{z}\sin\theta_i\, e^{jkz\cos\theta_i} E_o \sum_{n=0}^{\infty} \epsilon_n j^n \cos n(\phi_i-\phi)$$

$$\frac{J_n(\beta\rho)H_n^{(2)}(\beta a)-J_n(\beta a)H_n^{(2)}(\beta\rho)}{H_n^{(2)}(\beta a)} \tag{38}$$

where $\beta = k\sin\theta_i$ and a is the radius of the cylinder

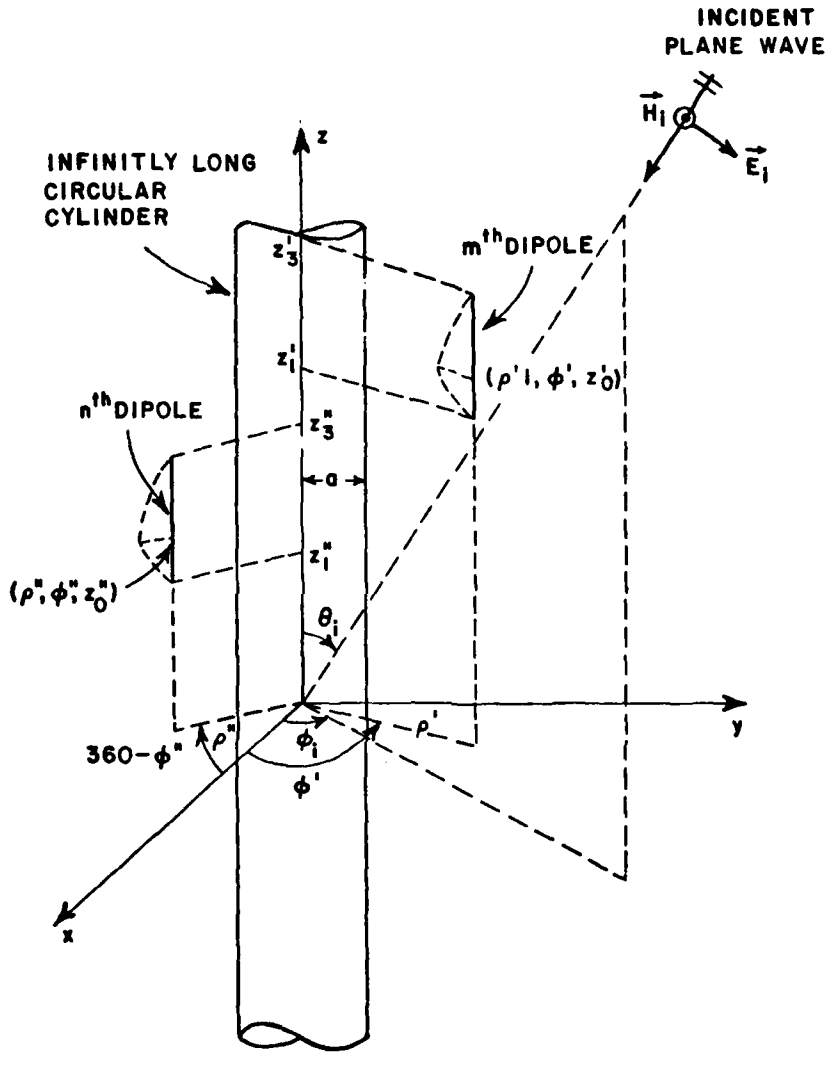

Figure 8. Principle geometry used for axial dipole calculations.

$$\varepsilon_n = \begin{cases} 1 & n=0 \\ 2 & n\neq 0 \end{cases}$$

In Appendix A various components of the fields are given in terms of E_z and H_z for TM_z and TE_z polarizations respectively.

It can be seen from these equations that, for TM_z case, H_ϕ is given as follows

$$H_\phi = -\frac{j\omega\varepsilon_o}{\beta^2}\frac{\partial E_z}{\partial \rho} \tag{39}$$

Then with the aid of Equation (21) and Equation (39), on the surface of the cylinder, isolated induced surface current density $\overline{J}_s = \hat{n}x\hat{\phi}H_\phi(a,z,\phi)$ is found to be

$$\overline{J}_s^o = -\hat{z}\frac{2}{\pi a}\frac{\omega\varepsilon_o}{k^2}\frac{e^{jkz\cos\theta_i}}{\sin\theta_i} E_o \sum_n \varepsilon_n j^n \frac{\cos n(\phi_i-\phi)}{H_n^{(2)}(\beta a)} \tag{40}$$

where $\beta = k\sin\theta_i$.

The isolated induced surface charge density ρ_s^o is determined from the equation of continuity.

$$\rho_s^o = \cos\theta_i \frac{2}{\pi a}\frac{\varepsilon_o}{k}\frac{e^{jkz\cos\theta_i}}{\sin\theta_i} E_o \sum_n \varepsilon_n j^n \frac{\cos n(\phi_i-\phi)}{H_n^{(2)}(\beta a)} \tag{41}$$

b. Current Magnitudes On the Dipoles

As indicated before, current magnitudes on the dipoles which are approximating the additional scatterers are found by moment method techniques. In order to solve for currents, I_m, from Equation (31), [Z] and (V) matrices must be known.

(1) [Z] Matrix

Entries of the [Z] matrix are calculated from Equations (36c) and (33b). By virtue of Equation (33b), the quantities Z_{mn}^o and ΔZ_{mn} for the axial dipole are

$$Z^{o}_{mn} = - \int_{z'_1}^{z'_3} dz' \int_{z''_1}^{z''_3} dz'' \, \overline{F}_m(z'') \cdot \overset{\approx}{E}_o(\overline{r}''|\overline{r}') \cdot \overline{F}_n(z') \tag{42}$$

and

$$\Delta Z_{mn} = - \int_{z'_1}^{z'_3} dz' \int_{z''_1}^{z''_3} dz'' \, \overline{F}_m(z'') \cdot \overset{\approx}{E}_s(\overline{r}''|\overline{r}') \cdot \overline{F}_n(z') \tag{43}$$

In the above equations, sinusoidal current distributions are used as basis functions,

$$\overline{F}(z) = \hat{z} \left\{ P_1 \frac{\sin k(z-z_1)}{\sin k d_1} + P_2 \frac{\sin k(z_3-z)}{\sin k d_2} \right\} \tag{44}$$

where

$$P_1 = \begin{cases} 1 & z_1 < z < z_o \\ 0 & \text{elsewhere} \end{cases}$$

$$P_2 = \begin{cases} 1 & z_o < z < z_3 \\ 0 & \text{elsewhere} \end{cases}$$

and

$$d_1 = |z_1 - z_o|$$

$$d_2 = |z_o - z_3|$$

z_1, z_o, z_3 and $\hat{z}$ are defined in Figure 9.

$\overset{\approx}{E}_s(\overline{r}''|\overline{r}') \cdot \hat{z}''$ is the scattered electric field from the infinitely long circular cylinder and is calculated at point $\overline{r}''$ when an infinitesimal axial dipole located at point $\overline{r}'$ is radiating in the presence of the cylinder. $\overset{\approx}{E}_s(\overline{r}''|\overline{r}')$ can be written in terms of dyadic electric Green's function as

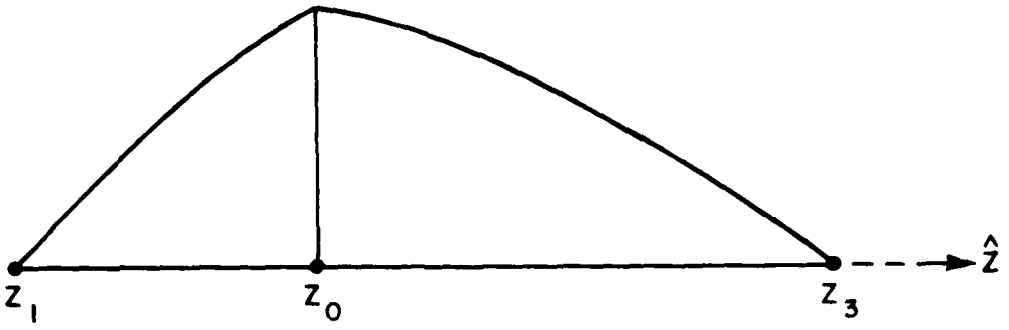

Figure 9. A linear test dipole and its sinusoidal current distribution. The endpoints are at z_1 and z_3 with terminals at z_0.

$$\tilde{\tilde{E}}_s(\bar{r}''|\bar{r}') = -j\omega\mu_0 \tilde{\tilde{G}}_e^s(\bar{r}''|\bar{r}') \tag{45}$$

For an axial dipole, the only nonzero contribution to the impedance matrix comes from the $\hat{z}\hat{z}$ component of the dyadic Green's function, $G_{ezz}(\bar{r}'\ \bar{r}')$. From Appendix B, scattered part of $\hat{z}\hat{z}$ component of the dyadic Green's function $G^s_{ezz}(\bar{r}''\ \bar{r}')$ is found to be

$$G^s_{ezz}(\bar{r}|\bar{r}') = \frac{j}{4\pi}\int_0^\infty dt \sum_{n=0}^{\infty} \varepsilon_n \frac{k^2-t^2}{k^2}\cos k(z-z') \frac{J_n(a\alpha)}{H_n(a\alpha)} H_n(p\alpha)H_n(\rho'\alpha) \tag{46}$$

where $\alpha = \sqrt{k^2-t^2}$

and

$$\varepsilon_n = \begin{cases} 1 & n=0 \\ 2 & \text{otherwise} \end{cases}$$

$\tilde{\tilde{E}}_o(\bar{r}''|\bar{r}')\cdot\hat{c}$ is the electric field at point $\bar{r}''$ which is generated by a $\hat{c}$ oriented infinitesimal dipole located at point $\bar{r}'$ when it is radiating in the free space. Similar to scattered electric field, $\tilde{\tilde{E}}_s(\bar{r}''|\bar{r}')$, $\tilde{\tilde{E}}_o(\bar{r}''|\bar{r}')$ is also defined as follows:

$$\tilde{\bar{\bar{E}}}_o(\bar{r}''|\bar{r}') = -j\omega\varepsilon_o \tilde{\bar{\bar{G}}}_e^o(\bar{r}''|\bar{r}') \tag{47}$$

where $\tilde{\bar{\bar{G}}}_e^o(\bar{r}''|\bar{r}')$ is the free space dyadic Green's function and is given in Appendix C. Again, only nonzero contribution comes from the $\hat{z}\hat{z}$ component of $\tilde{\bar{\bar{G}}}_e^o(\bar{r}''|\bar{r}')$ which is given by

$$G_{ezz}^o(\bar{r}|\bar{r}') = \left(1 + \frac{1}{k^2}\frac{\partial^2}{\partial z^2}\right)\frac{e^{-jk|\bar{r}-\bar{r}'|}}{|\bar{r}-\bar{r}'|\,4\pi} \tag{48}$$

Now [Z] matrix can be written as

$$[Z] = \begin{bmatrix} Z_{11}^o & Z_{12}^o & \cdots & Z_{1N}^o \\ & \cdot & & \\ & \cdot & & \\ & \cdot & & Z_{NN}^o \end{bmatrix} + \begin{bmatrix} \Delta Z_{11} & \Delta Z_{12} & \cdots & \Delta Z_{1N} \\ & \cdot & & \\ & \cdot & & \\ & \cdot & & \Delta Z_{NN} \end{bmatrix} \tag{49}$$

(2) The Source (V) Matrix

(V) matrix is the summation of the isolated and perturbed open circuit voltages on the dipoles, i.e.,

$$(V) = \begin{pmatrix} V_1^o \\ V_2^o \\ \cdot \\ \cdot \\ \cdot \\ V_N^o \end{pmatrix} + \begin{pmatrix} V_1 \\ V_2 \\ \cdot \\ \cdot \\ \cdot \\ V_N \end{pmatrix} \tag{50}$$

The elements of these column matrices are calculated from Equation (33a)

$$V_m^o = \int_{z_1'}^{z_3'} E_z^i(\bar{r}')\, F_m(z')dz' \tag{51}$$

and

$$\Delta V_m = \int_{z_1'}^{z_3'} E_z^s(\bar{r}')\, F_m(z')dz' \tag{52}$$

where E_z^s and E_z^i are the $\hat{z}$ components of the reflected electrical fields from the cylinder and the direct incident field respectively and are given by Equations (53), (54)

$$E_z^i(\bar{r}') = -\sin\theta_i\, E_o\, e^{jk(z'\cos\theta_i+\rho'\sin\theta'\cos(\phi_i-\phi'))} \tag{53}$$

and

$$E_z^s(\bar{r}') = \sin\theta_i\, E_o\, e^{jkz'\cos\theta_i} \sum_{n=0}^{\infty} \varepsilon_n j^n \cos n(\phi_i-\phi') \frac{J_n(\beta a)}{H_n(\beta a)} H_n(\beta\rho') \tag{54}$$

where $\beta = k\sin\theta_i$

$F_m(z)$ is the magnitude of $\bar{F}(z)$ which is given in Equation (44).

Now the currents on the dipoles can be found by simply inverting [Z] matrix and multiplying by the (V) matrix

$$(I) = [Z]^{-1}\,(V) \tag{55}$$

c. Currents and Charges Due to Dipoles

Perturbed surface current and charge densities induced on the cylinder is the result of the currents on the dipoles which are modeling the additional scatterers. The magnitudes of these currents on the dipoles and in turn, the whole current distribution,which is approximated by sinusoidal basis functions, on the additional scatterers is already found in step 2. In order to calculate the perturbed surface induced current density, it is necessary to find the tangential magnetic field on the surface of the cylinder. For an axial dipole the z component of the magnetic field is zero. From Appendix A, it is easy to see that for TM_z case H_ϕ and E_z are related to each other by the following equation.

$$H_\phi = -\frac{j\omega\epsilon_o}{\beta^2}\frac{\partial E_z}{\partial \rho} \tag{56}$$

For a radial dipole with a sinusoidal current distribution on it as shown in Figure 9, the $\hat{z}$ component of the electrical field can be found from Equation (13) as follows:

$$E_z^m = -j\omega\mu_o I_m \int_{z_1'}^{z_3'} F_m(z')G_{ezz}(\bar{r}|\bar{r}')dz' \tag{57}$$

where I_m is the current magnitude or the m^{th} dipole. E_z^m is the $\hat{z}$ component of the electric field generated by the same dipole.

$G_{ezz}(\bar{r}|\bar{r}')$ is the $\hat{z}\hat{z}$ component of the dyadic Green's function and, from Appendix B, is found to be

$$G_{ezz}(\bar{r}|\bar{r}') = -\frac{\dot{d}}{4\pi}\int_o^\infty dt \sum_{n=0}^{\infty} \epsilon_n \frac{k^2-t^2}{k^2}\cos t(z-z')\frac{H_n(\rho'\alpha)}{H_n(a\alpha)}$$

$$\cos n(\phi-\phi')\left\{J_n(\rho\alpha)H_n(a\alpha) - J_n(a\alpha)H_n(\rho\alpha)\right\} \tag{58}$$

H_ϕ can be calculated by sustituting Equation (58) into Equation (57) and then substituting Equation (57) into Equation (56). Once H_ϕ is found, then the perturbed induced surface current density, $\Delta\bar{J}_m$, (due to the m^{th} dipole is found from the boundary condition. The equation of continuity can be used in order to find the perturbed induced surface charge density $\Delta\rho_m$. The resulting expressions for $\Delta\bar{J}_m$ and $\Delta\rho_m$ are given in Equations (59) and (60).

$$\Delta\bar{J}_m = -\hat{z}\, I_m \int_{z_1'}^{z_3'} \frac{F(z')dz'}{2\pi^2 a}\int_o^\infty dt \sum_{n=0}^{\infty} \epsilon_n \cos t(z-z')\frac{H_n(\rho'\alpha)}{H_n(a\alpha)}\cos n(\phi-\phi') \tag{59}$$

and

$$\Delta\rho_m = I_m \int_{z_1'}^{z_3'} \frac{F(z')dz'}{2\pi^2 a} \int_0^\infty dt \sum_n t\,\varepsilon_n \sin t(z-z') \frac{H_n(\rho'\alpha)}{H_n(a\alpha)} \cos n(\phi-\phi) \tag{60}$$

In the above equations prime coordinates indicate the source location and unprime coordinates indicate the observation point. In order to arrive at Equations (59) and (60), the following Wronskian relation is also used.

$$J_n'(x)\,H_n(x) - J_n(x)\,H_n'(x) = \frac{2j}{\pi x} \tag{61}$$

d. Total Induced surface Charge and Current Densities

The results found in steps 1 and 3 with the combination of superposition theorem enable us to calculate the total induced surface charge and current densities on the surface of the cylinder.

$$\bar{J}_s = \bar{J}_s^o + \sum_{m=1}^{N} \Delta\bar{J}_m \tag{62}$$

$$\rho_s = \rho_s' + \sum_{m=1}^{N} \Delta\rho_m \tag{63}$$

2. Results

Results obtained using the techniques outlined in the previous section are to be presented in this section. Wherever practical, the computations are verified at each step in the process by a completely different solution to establish confidence not only in the technique itself, but also the computer programs used to obtain the results.

While there are no known results giving the impedances, the currents and voltages induced on the scatterers, some related geometries can be treated that will approximate the same results. One of these is the case of a horizontal dipole mounted over an infinite ground plane which can be analyzed by image theory. This case can be related to the case of a horizontal dipole close to the surface of a cylinder as compared to the radius of the cylinder.

A second geometry that can easily be treated is that of a dipole near a very thin finite length cylinder. Here, the length of the thin cylinder can be made sufficiently long that it gives the same results for the impedances on the wires representing the wing. A moment method solution can then be used to obtain the fields of this finite length relatively long thin cylinder in the presence of a thin short wire. This result can then be compared to those obtained using the hybrid formulation of major interest.

The agreement between these geometries is given in the following paragraphs. First the impedance of a short dipole is examined, second the open circuited voltage at the dipole is presented, third the near field results for an axial short dipole in the presence of an infinite cylinder are given and, finally, the total perturbed and isolated surface current densities on the infinite cylinder are presented.

The following is organized into four subsections:

a. Impedance Matrix [Z] Results

b. Voltage Matrix [V] Results

c. Charge and Current Densities Induced on an Infinite Cylinder by a Dipole Source

d. Surface Current Densities on the Cylinder.

Actually, the impedances are the mathematical representation of the total geometry and are all that are needed for the analysis of the surface current and charge densities on the cylinder. However to ascertain that the current and charge densities on the wings themselves are valid, it appears to be of some merit to demonstrate that the voltages and currents existing on the dipoles are also correct. Of course, the important quantity in evaluating the current density induced on the surface of the cylinder is the total current on the dipole elements; the impedance and driving voltages merely represent part of the process of correctly evaluating the currents on these dipoles.

The main purpose of the following paragraphs is to establish the validity of the computer programs obtained from the newly derived equation. Once the correctness of these results is demonstrated, then the acceptability of the rest of the elements follows from the well established moment method techniques and the superposition theorem.

a. Impedance Matrix [Z] Results

The validity of Equations (42), (43), and (49) for the impedance of a short dipole in the vicinity of the incident cylinder is examined. Equation (42) is a well known expression and is widely used in regular moment method solutions. Richmond [22], et al. write Equation (42) in a more familiar form

$$Z^o_{mn} = - \int d\bar{r}' \; \bar{J}_m(\bar{r}') \cdot \bar{E}_n(\bar{r}') \tag{64}$$

where $\bar{E}_n(\bar{r}')$ is the electrical field generated by the nth dipole when it is radiating in the homogeneous medium (μ_o, ε_o) without the other wires and the infinite cylinder present, and this electrical field is calculated at the location of the mth dipole. It can easily be seen from Equations (42) and (64) that

$$\bar{E}_n(\bar{r}') = \int \bar{\bar{E}}^s_o(\bar{r}'|\bar{r}') \cdot \bar{F}_n(\bar{r}'') \, d\bar{r}'' \tag{65}$$

Figures 10, 11 and 12 are plots of the real and imaginary parts of the total self-impedance ($Z_{mm} = Z^o_{mm} + \Delta Z_{mm}$) of a dipole in the presence of an infinitely long cylinder versus the distance, H, of the dipole from the surface of the cylinder. Equations (42) and (43) are used in order to calculate Z^o_{mm} and ΔZ_{mm} respectively. The same plots present the results obtained when infinite groundplane replaces the cylinder. As has been noted, the infinite ground plane calculations are made by finding the self impedance of the dipole in the absence of the infinite ground plane (Z^o_{mm}) and adding to this the mutual impedance between the dipole and its image ($Z^o_{mm'}$) so that

$$Z_{mm} = Z^o_{mm} + Z^o_{mm'} \tag{66}$$

where m' is the image location. Both Z^o_{mm} and $Z^o_{mm'}$ are calculated from Equation (42). Observe that $Z^o_{mm'}$ is the approximation to Z_{mm} obtained by replacing the infinite cylinder by the infinite ground plane.

In the case of a cylinder with a large radius (Figures 10 and 11), the results obtained by Equation (43) and the results found from the infinite ground plane are in reasonable agreement when the dipole is close to the surface of the cylinder. This is an expected result because, insofar as the dipole impedance is concerned, the cylinder appears as if it were an infinite ground plane. The data presented

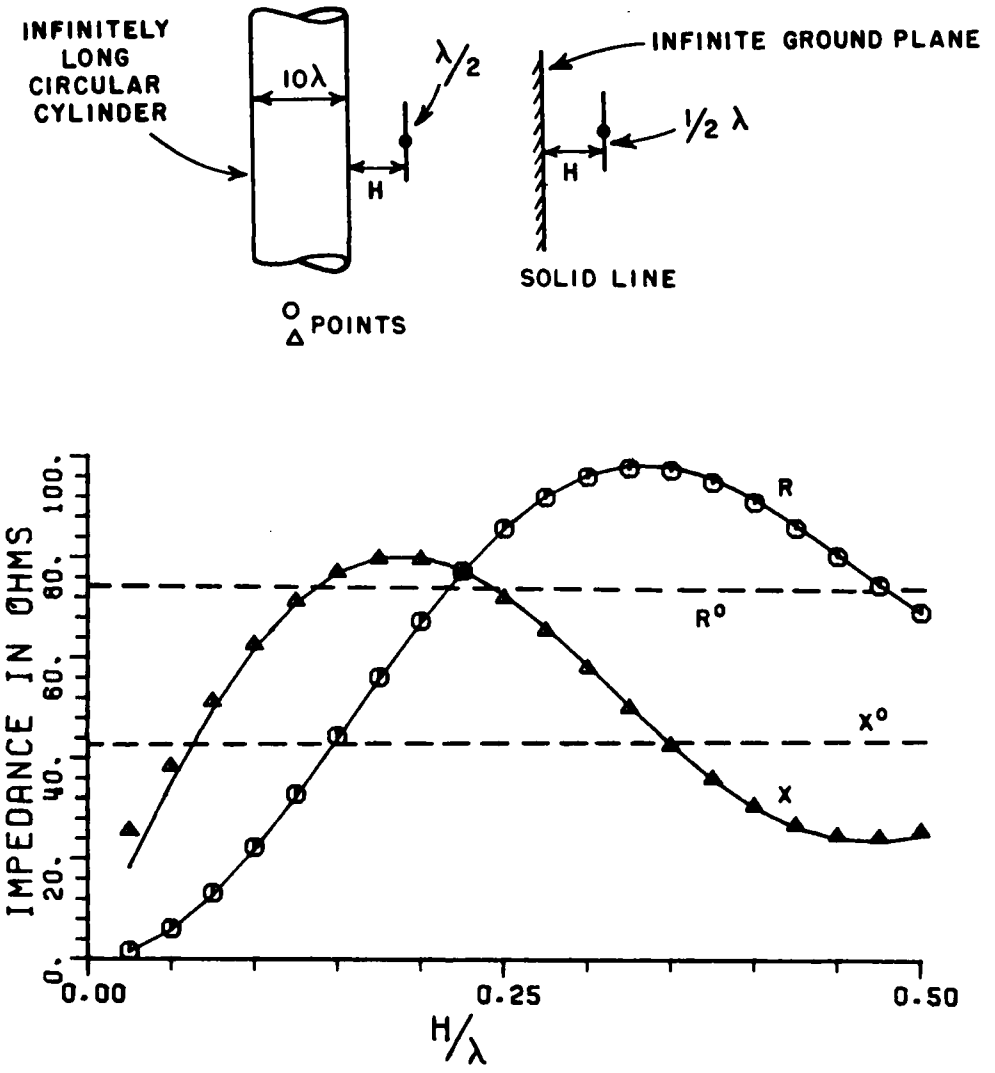

Figure 10. Input impedance of a half wavelength axial dipole near an infinitely long circular cylinder with 5 λ radius.

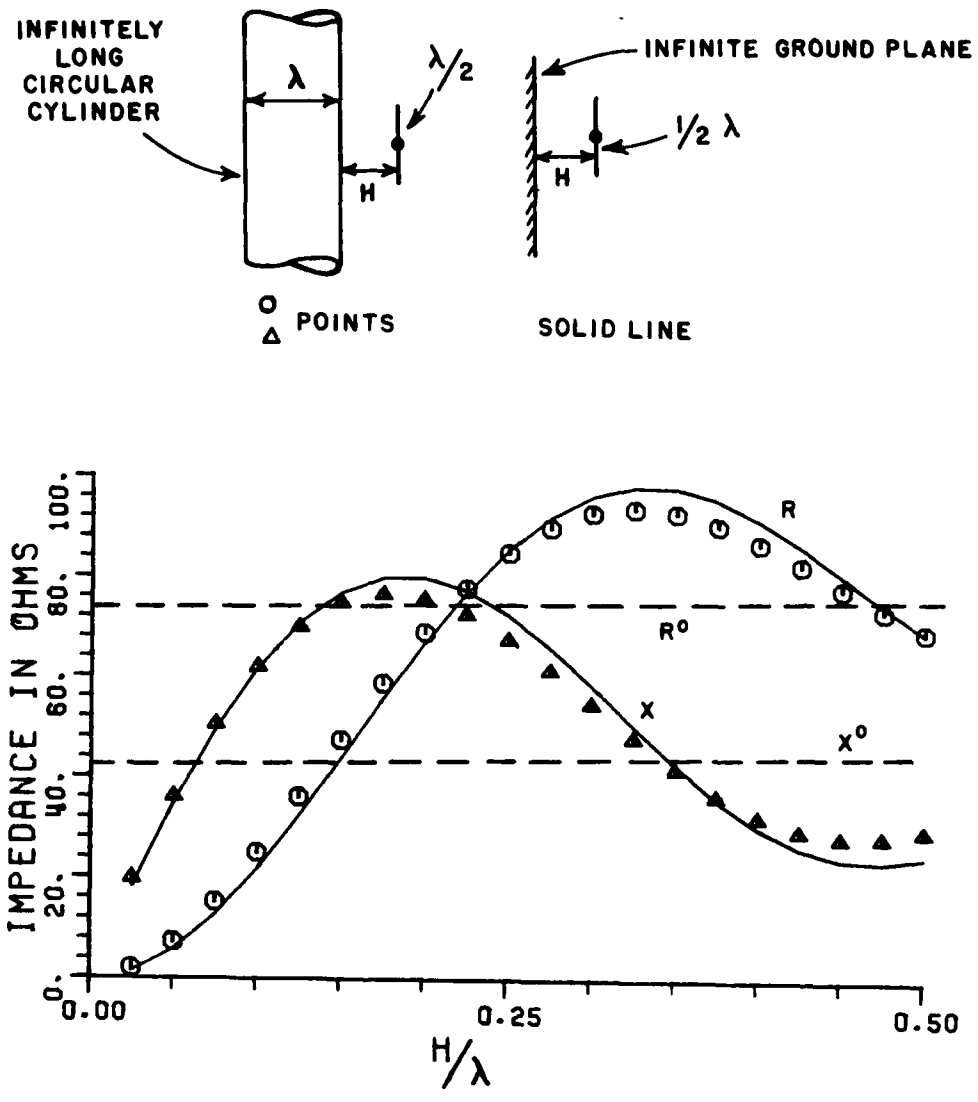

Figure 11. Input impedance of a half wavelength axial dipole near an infinitely long circular cylinder with 0.5λ radius.

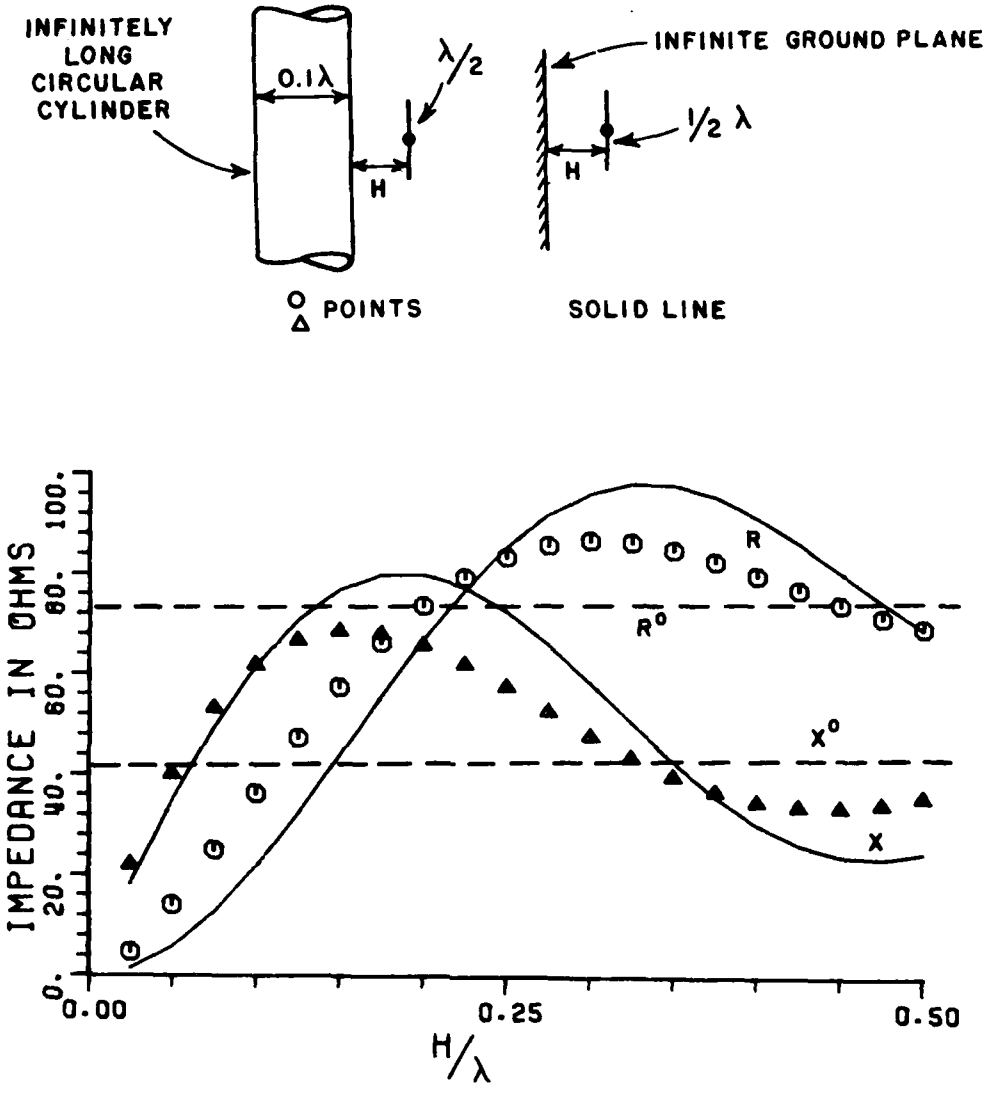

Figure 12. Input impedance of a half wavelength axial dipole near an infinitely long circular cylinder with 0.05λ radius.

in Figure 12 are also satisfactory since the ground plane does not closely approximate a cylinder whose radius is only 0.05λ.

Figures 13, 14 and 15 are used to compare the results obtained from regular moment method techniques with the results obtained from Equation (43). The hybrid solution is seen to be valid by these computations and indeed the derivatives observed earlier when the ground plane replaced the 0.05λ cylinder (Figure 12) is now clearly seen to be caused by the change in geometry. Note that the results presented in Figures 14 and 15 are obtained for different length dipoles. The agreement between results obtained from the two solutions is more than satisfactory. At this point, it is claimed that the impedance computations using the hybrid solutions for both large radii cylinders (Figures 10,11,12) and small radii cylinders (Figures 13,14,15) are correct.

Up to this point the validity of Equation (43) is checked when "n=m" in other words for self impedance, Z_{mm}, calculations. The mutual impedance between two dipoles in the presence of the infinite cylinder has been calculated from Equation (43). The results are shown in Figures 16, 17, 18 and 19. As has been done for the self impedance calculations, mutual impedance calculations are also compared to infinite ground plane and regular moment method solutions. In Figures 16 and 17, the differential component of the mutual impedance between two dipoles caused by the presence of the cylinder (the perturbed mutual impedance, ΔZ_{12}) is presented. This perturbed mutual impedance is compared to the value obtained when the cylinder is replaced by the infinite ground plane.

In Figures 18 and 19, the change in the mutual impedance of two dipoles caused by the presence of a thin cylinder is plotted. On the same graphs, the moment method solution is presented. For moment method solution, the thin cylinder is modeled as a finite length thin wire of the same radius.

Figures 16, 17, 18 and 19 clearly establish the accuracy of Equations (43) in predicting the mutual impedance. The only point where near perfect agreement is not obtained is for the large cylinder (R=5.0λ) when the two dipoles are arranged in a near endfire configuration.

b. Voltage Matrix ($\overline{V}$) matrix

The accuracy of Equations (51) and (52) for the source voltages or the dipoles is tested in the folloiwng paragraphs. As was Equation (42), Equation (51) is also a well known expression and is used in the regular moment method solutions. The accuracy of Equations (52), on the other hand, should be verified. This is the goal of Figures 20 and 21. It is expected that when the radius of the cylinder is large compared to the distance, H, between the dipole and the surface of the cylinder then the cylinder should appear as if it were an infinite

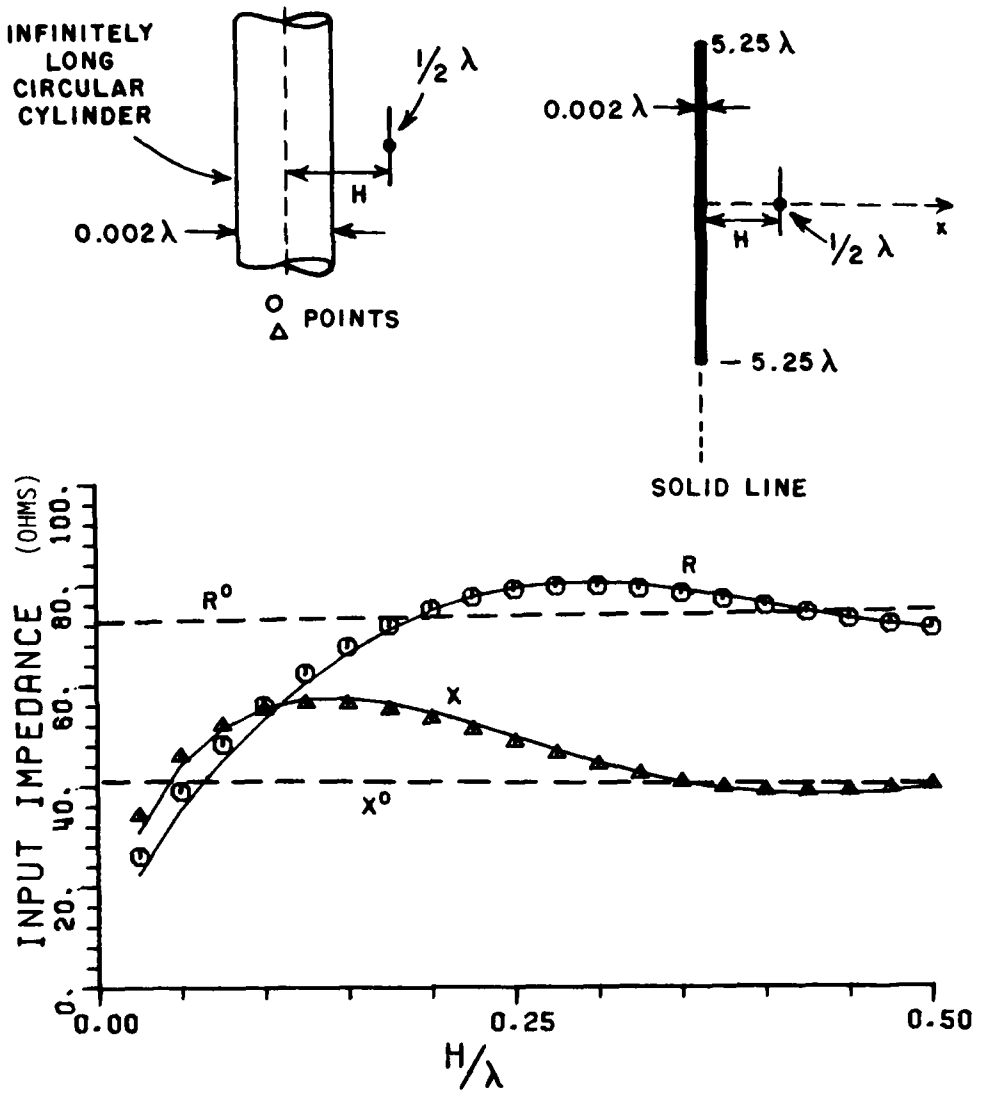

Figure 13. Input impedance of a half wavelength axial dipole near an infinitely long circular cylinder with 0.001λ radius.

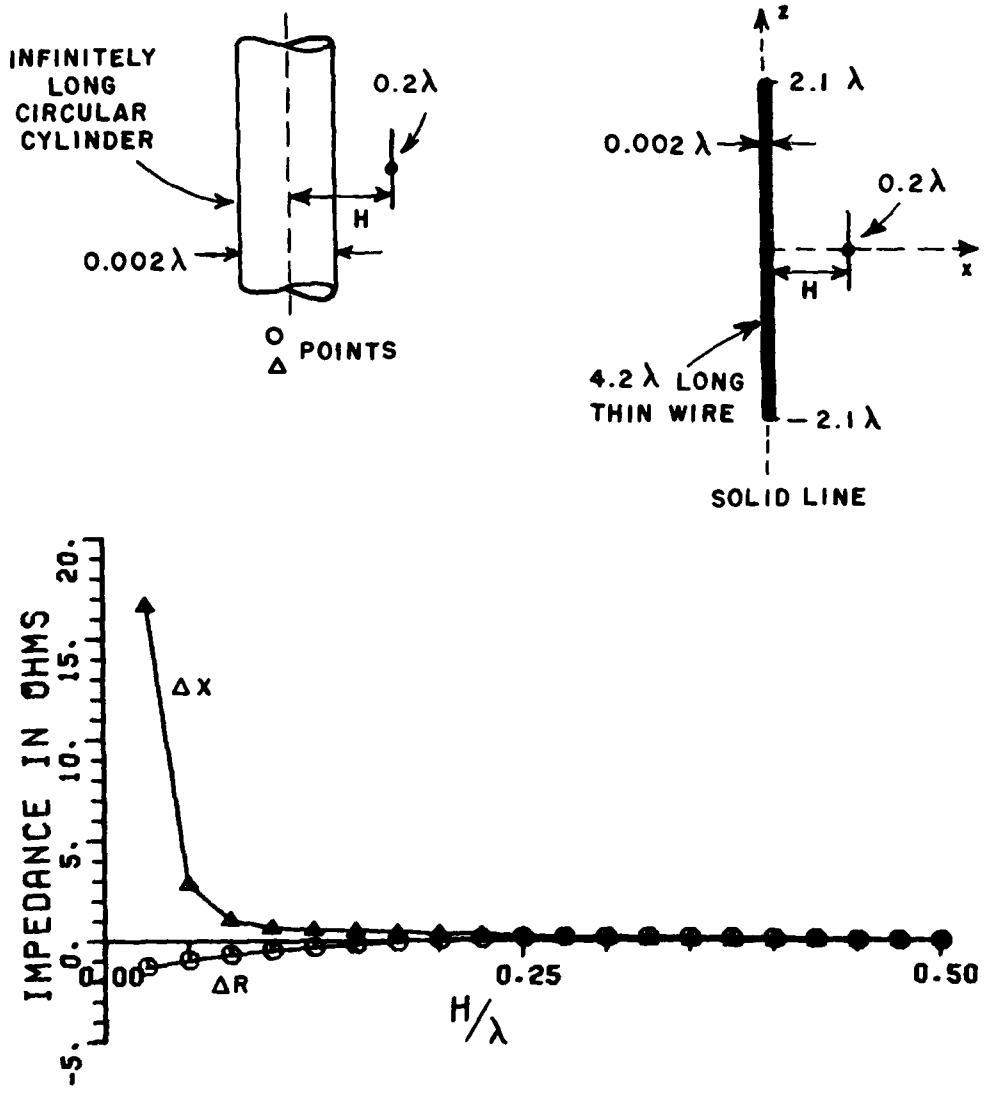

Figure 14. Perturbed impedance of a 0.2λ axial dipole near an infinitely long circular cylinder with 0.001λ radius.

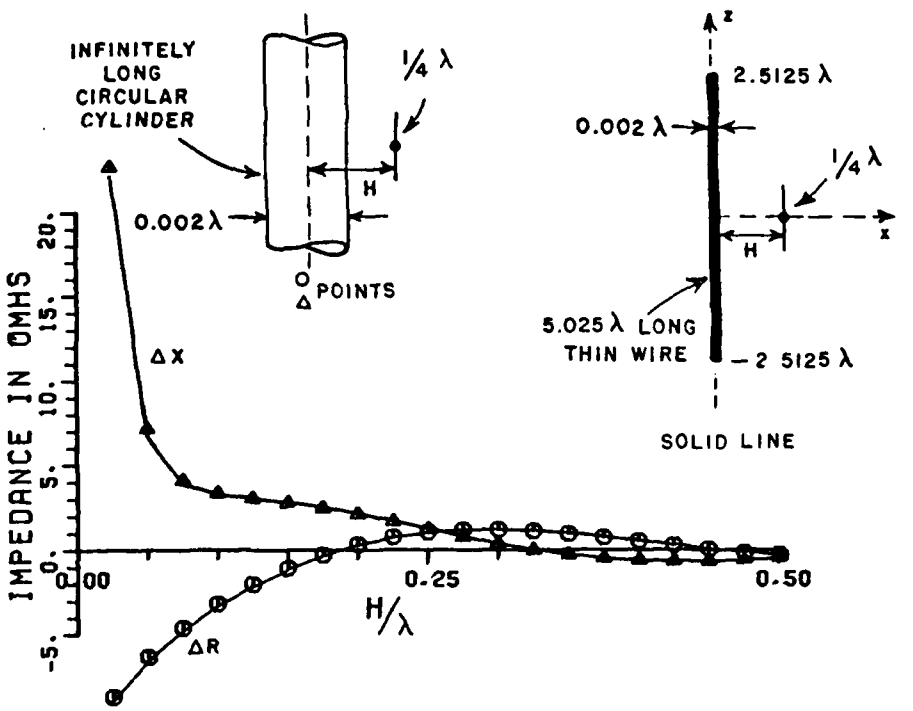

Figure 15. Perturbed impedance of a 1/4λ axial dipole near an infinitely long circular cylinder with 0.001λ radius.

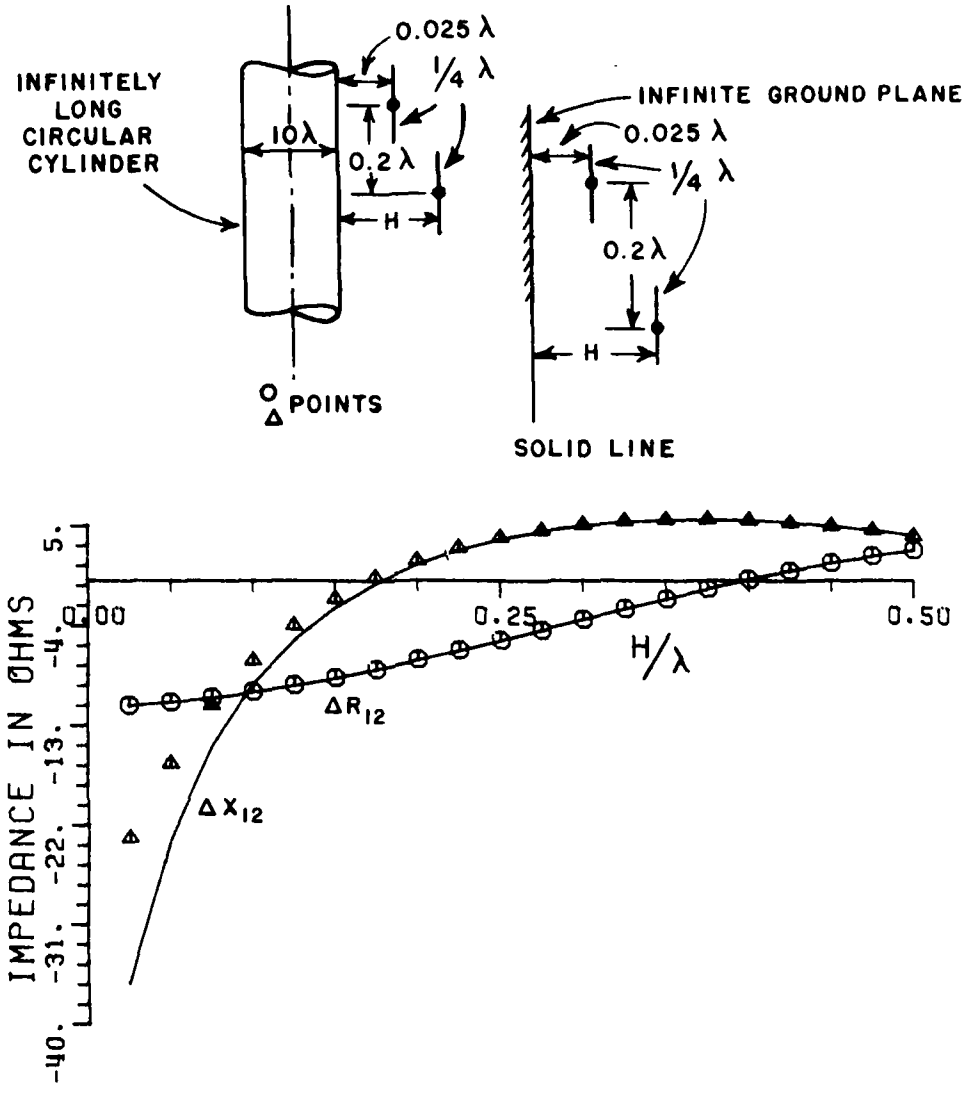

Figure 16. Mutual perturbed impedance between two 1/4λ axial dipoles near an infinitely long circular cylinder with 5λ radius.

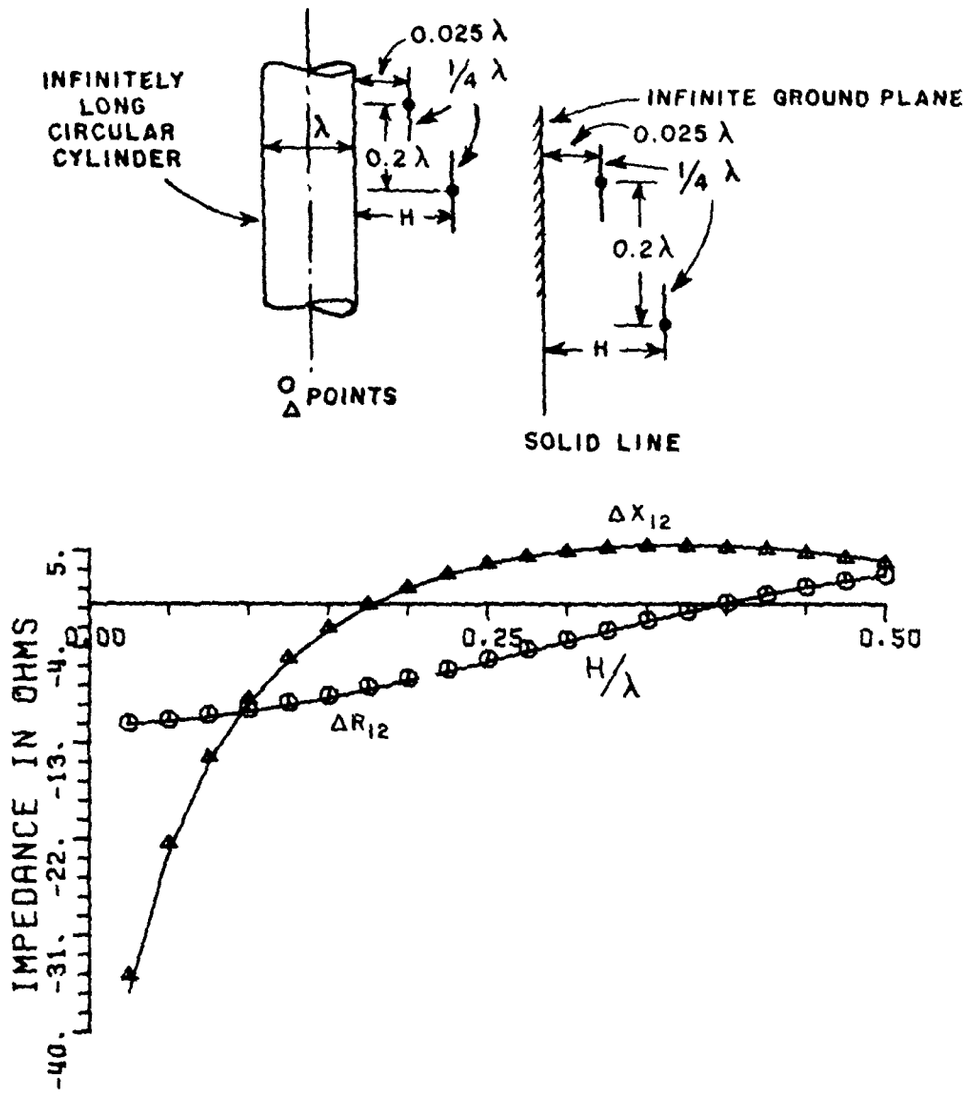

Figure 17. Mutual perturbed impedance between two 1/4λ axial dipoles near an infinitely long circular cylinder with 0.5λ radius.

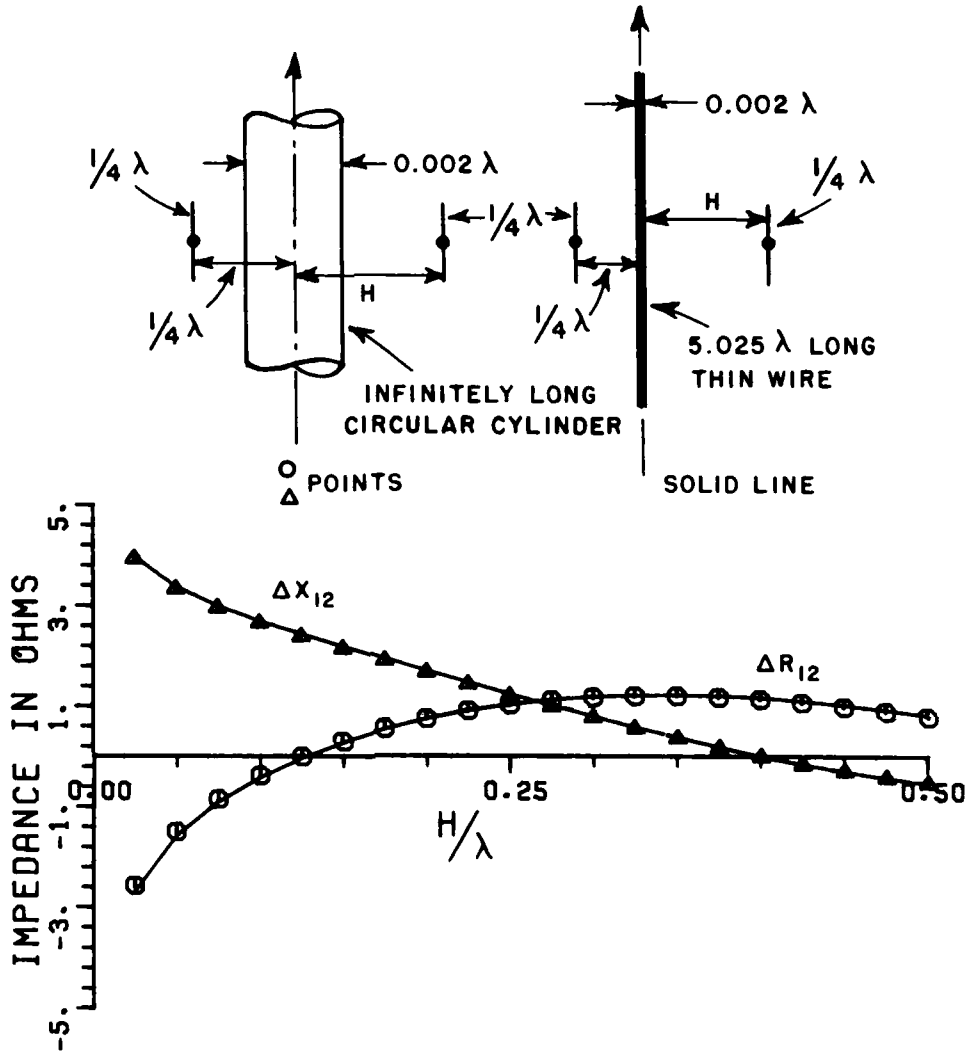

Figure 18. Perturbed mutual impedance between two 1/4λ axial dipoles near an infinitely long circular cylinder with 0.001λ radius.

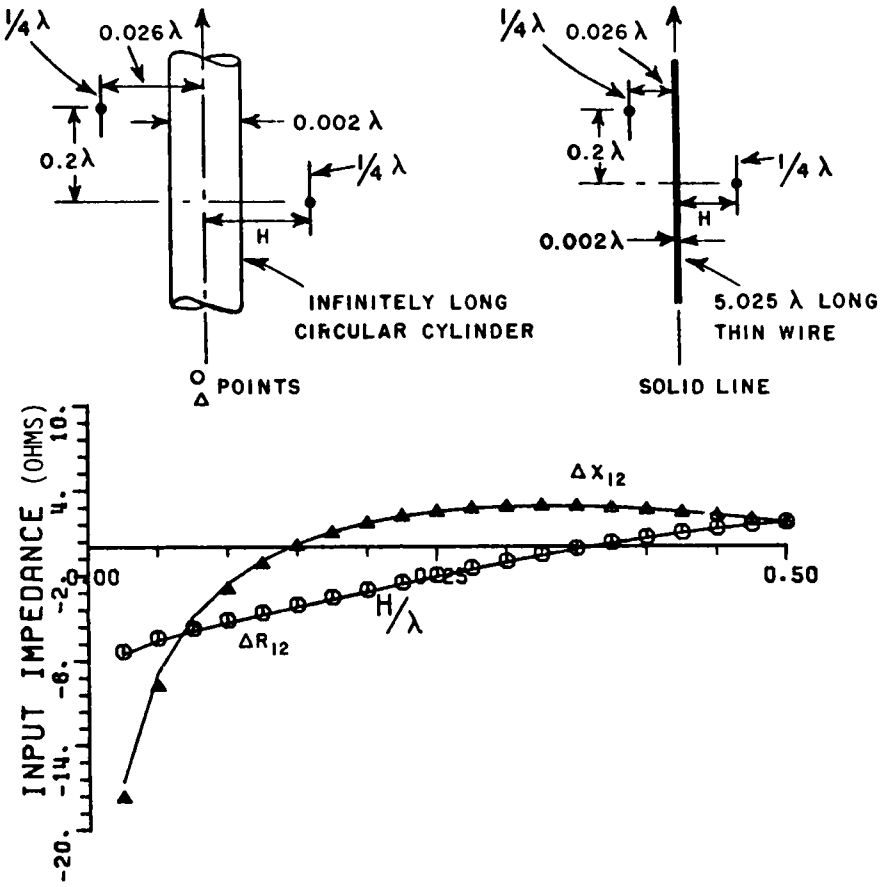

Figure 19. Perturbed mutual impedance between two 1/4λ axial dipoles near an infinitely long circular cylinder with 0.001λ radius.

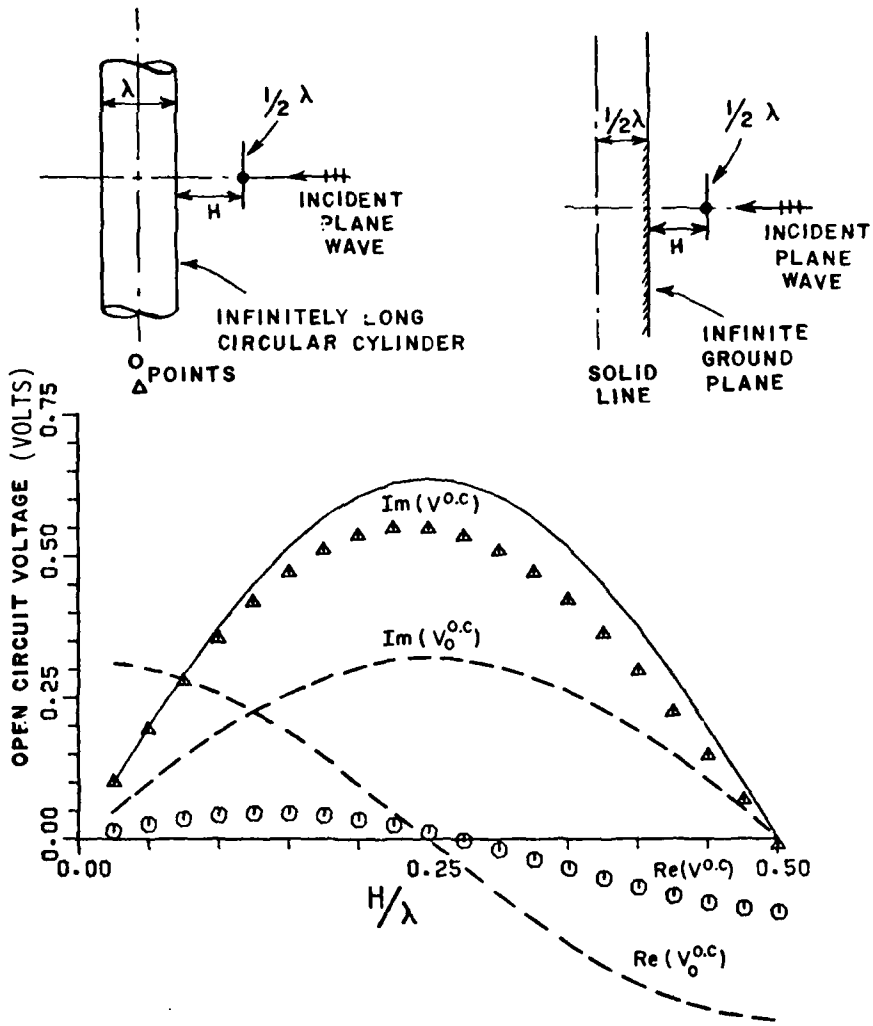

Figure 20. Open circuit voltage at the terminals of a 1/2λ axial dipole near an infinitely long circular cylinder with 0.5λ radius for a broadside plane wave incident. $V_o^{o.c}$ denotes the isolated open circuit voltage.

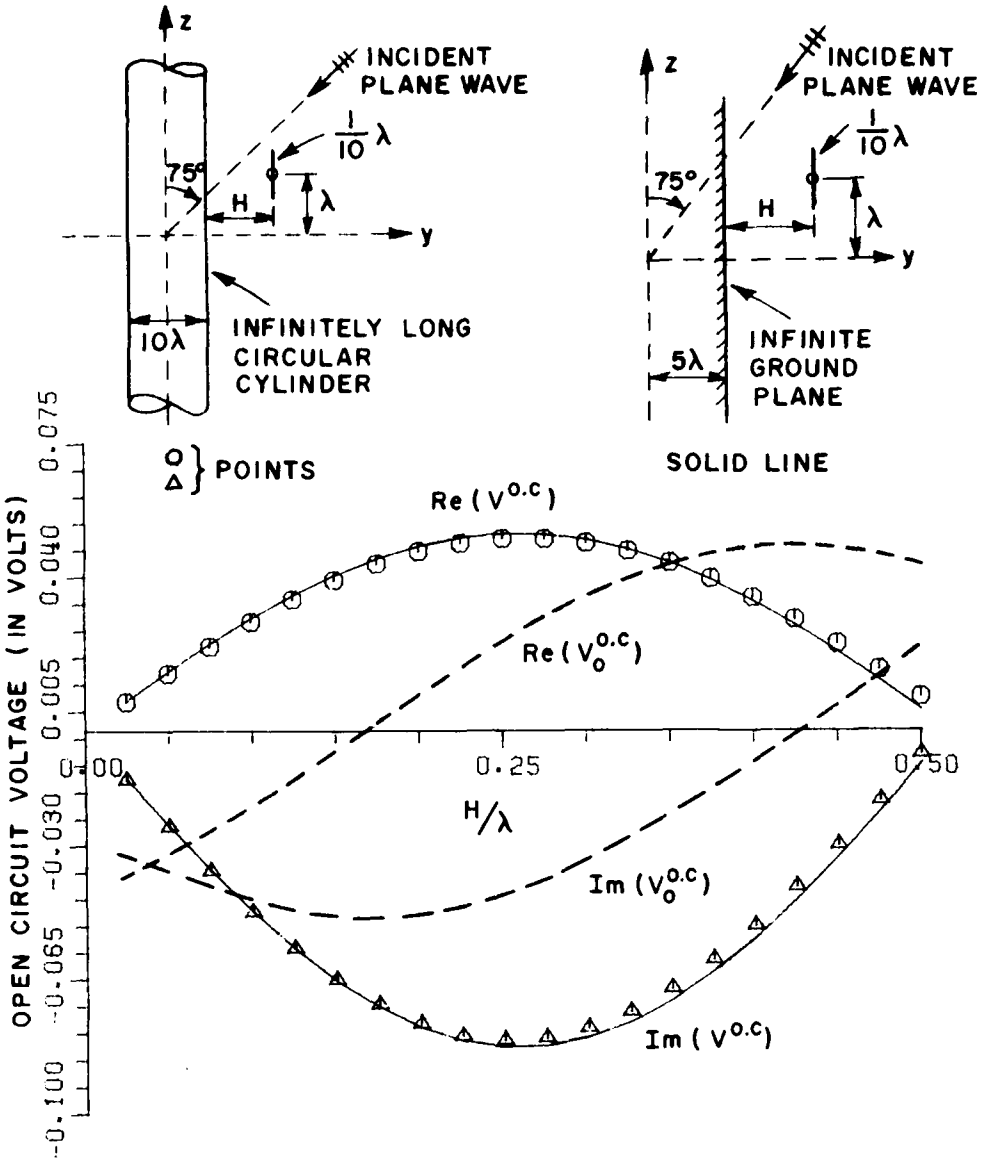

Figure 21. Open circuit voltage at the terminals of a 1/10λ axial dipole near an infinitely long circular cylinder with 5λ radius for an oblique incident plane wave. $V_o^{o.c.}$ denotes the isolated open circuit voltage.

ground plane. Indeed, this is the conclusion one could draw from Figures 20 and 21. Figure 21 is included here in order to demonstrate the fact that in the case of oblique plane wave incident, the results obtained from the equations in this report are still valid for an axial wire.

This concludes the verification of [Z] and (V) matrices. The results obtained from newly derived equations (Equations (43) and (52)) are satisfactory. Hence, as the final step on the regular moment method solution, now Equation (31) can safely be used in order to find the correct currents on the dipoles modeling the additional scatterers. Since the validity of regular moment method solutions is checked over and over again, it is excepted, in this thisis, that the currents calculated from Equation (31) on the dipoles are correct and there is no need to make any further verification.

c. Charge and Current Densities Induced on an Infinite Cylinder by a Dipole Source

As has been noted, the total induced surface current and charge densities are the sum of the isolated and perturbed surface current and charge densities. In the case of the perturbed quantities, the dipole of interest, say mth dipole, is taken as the source of the radiation. The current on this dipole is assumed to be sinusoidally distributed with unit magnitude at the terminals of the dipole. The resulting induced surface current and charge densities on the cylinder are called the perturbed surface current and charge densities and can be calculated from Equations (59) and (60) by setting I_m=1. In order to calculate the total induced surface current and charge densities on the surface of the cylinder, these perturbed quantities must be multiplied by terminal currents as calculated from the moment method techniques. Figures 22 through 26 present some of the results obtained from Equations (59) and (60) with I_m=1.

d. Surface Current Densities on the Cylinder

In Figures 27 and 30, the total induced surface current densities are presented when there are one dipole and two dipoles in the vicinity of the infinite cylinder [25]. These graphs are obtained as follows: First the current magnitudes at the terminals of the dipoles are found from $(I) = [Z]^{-1} (V)$ relation. Next the perturbed surface current densities are calculated from Equation (59) with I_m=1. Then these perturbed surface current densities are multiplied by the correct current magnitudes at the terminals. Finally these results are combined with the isolated surface current densities to give the total surface current density induced on the infinite cylinder.

For one dipole case, perturbed and isolated induced surface current densities are also presented in Figures 28 and 29.

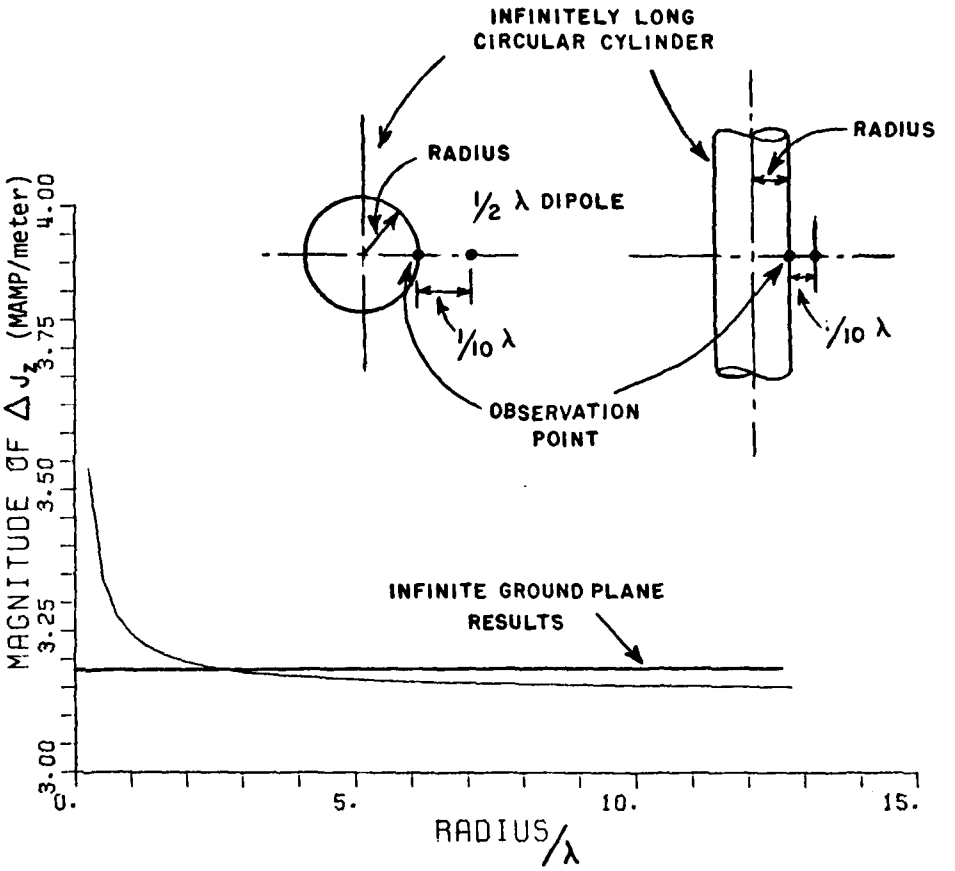

Figure 22. Magnitude of surface induced perturbed current on an infinitely long cylinder (I_m=1).

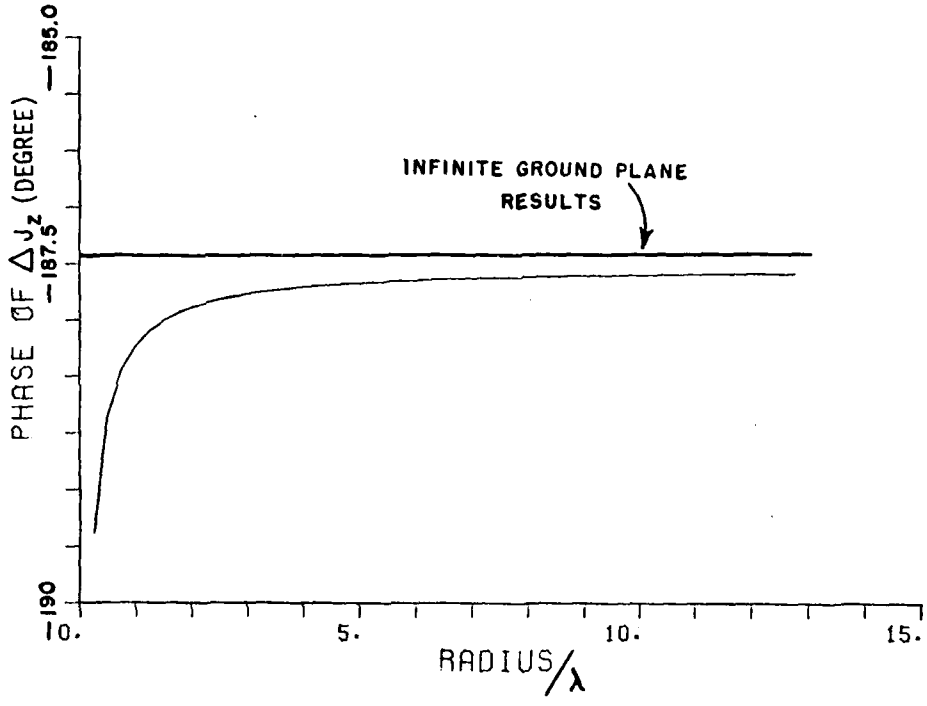

Figure 23. Phase of surface induced perturbed current on an infinitely long circular cylinder due to a 1/2 axial dipole excited with unit magnitude current located 1/10λ away from the surface of the cylinder.

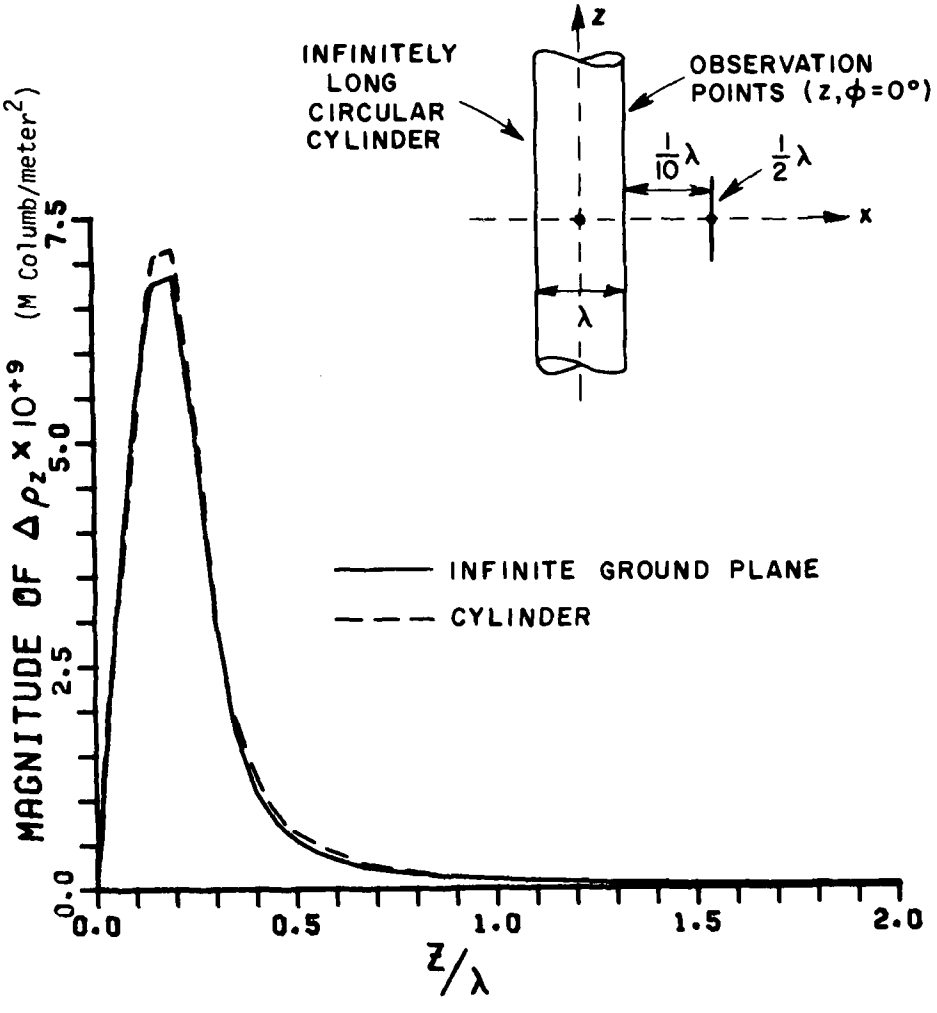

Figure 24. Magnitude of surface induced perturbed charge density on an infinitely long cylinder due to a 1/2λ dipole excited with unit magnitude current located 1/10λ away from the surface of the cylinder.

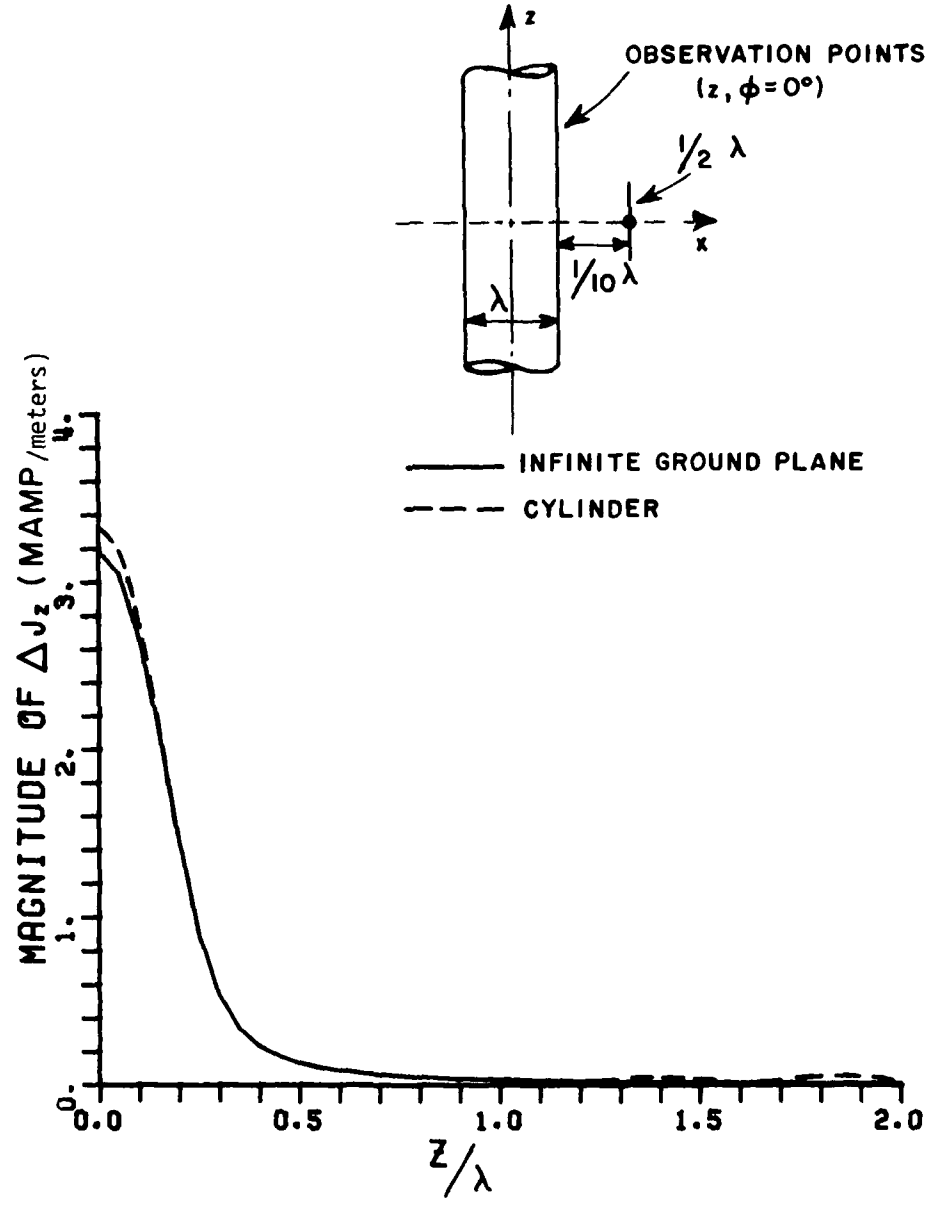

Figure 25. Magnitude of surface induced perturbed current density on an infinitely long circular cylinder with 1/2λ radius due to a 1/2λ dipole excited with unit magnitude current located 1/10λ away from the surface of the cylinder.

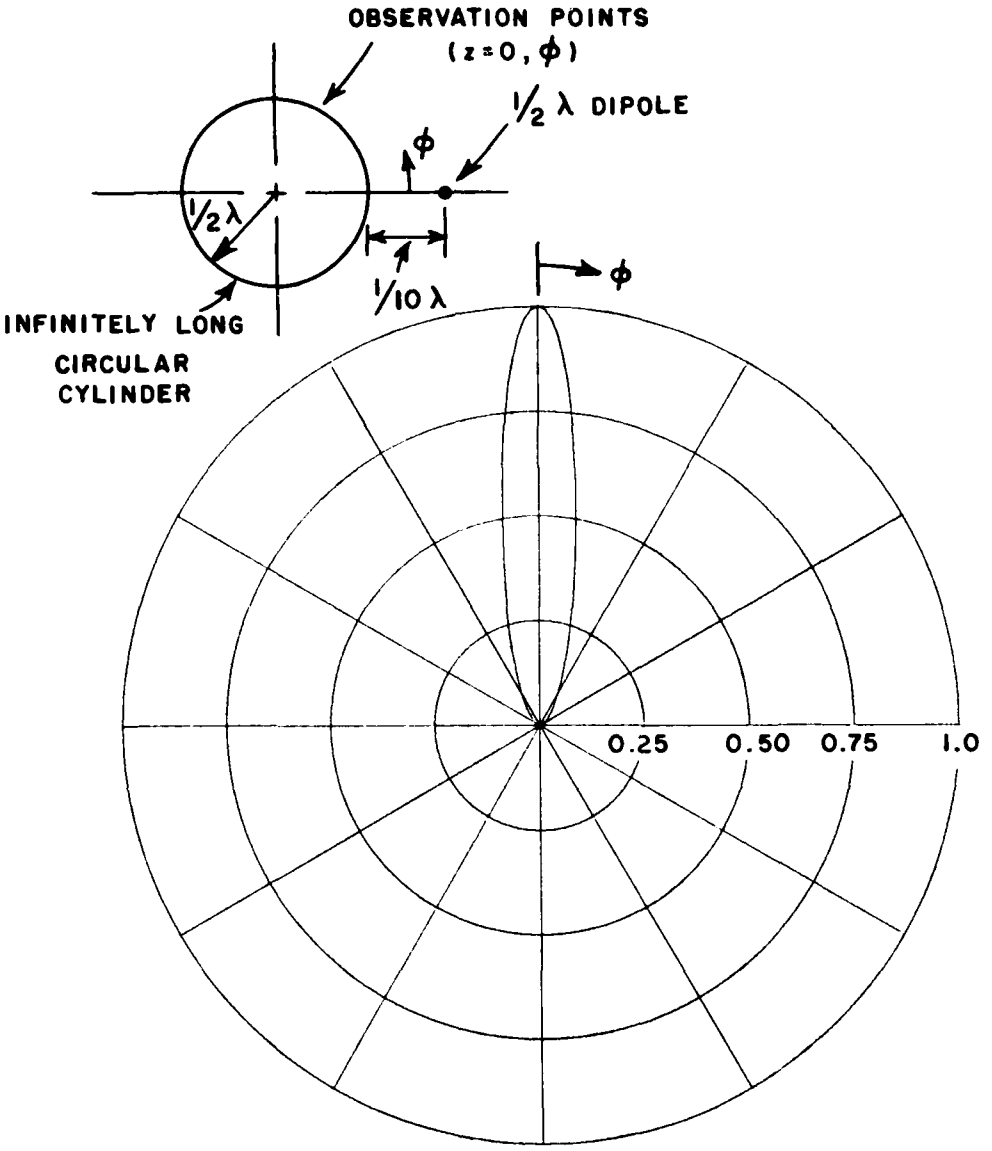

Figure 26. Surface induced perturbed current density on an infinitely long circular cylinder due to a dipole excited with unit magnitude current. Normalization factor is 3.34 mAmp/meter.

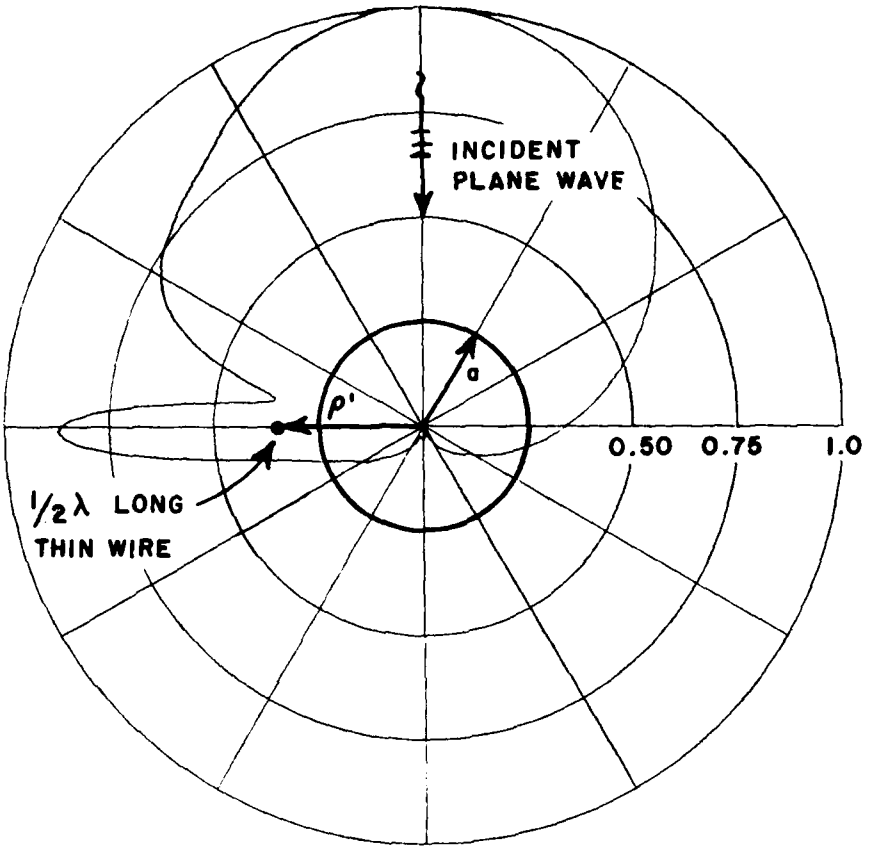

Figure 27. Normalized total surface current induced on an infinitely long circular cylinder with 1/2λ radius in the presence of a thin wire. ($J_z=J_z^0+\Delta J_s \cdot I_m$). Thin wire is located 1/10λ away from the cylinder. Normalization factor is 5.52 mAmp/meter. $|I_m|$=1.98 amps.

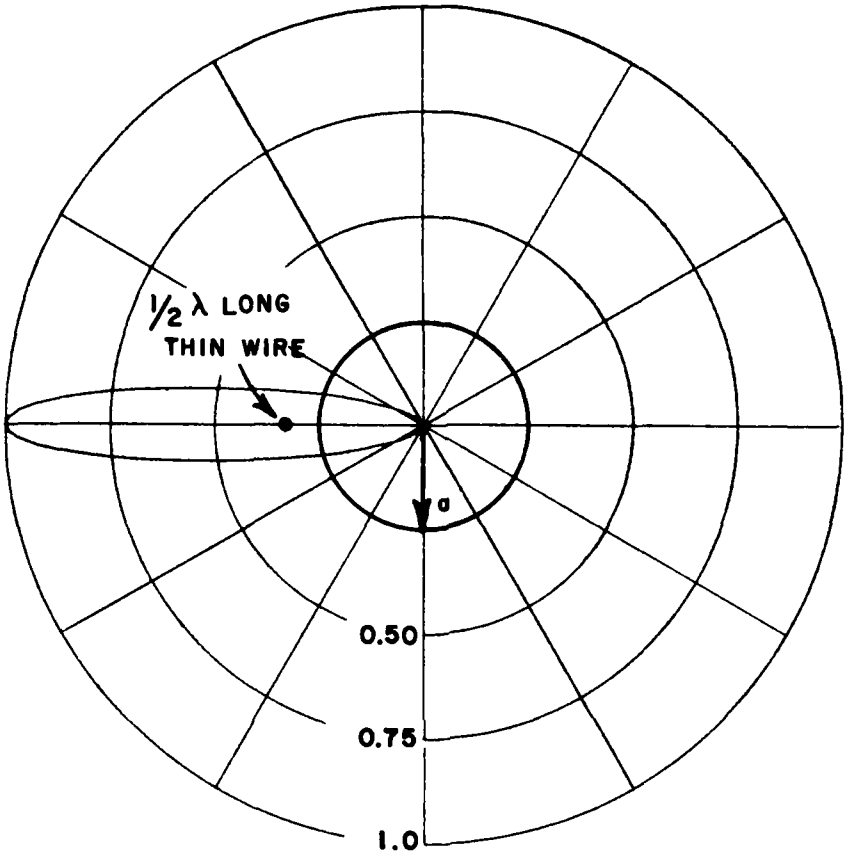

Figure 28. Normalized perturbed surface current density (ΔJ_z) for geometry of Figure 27.

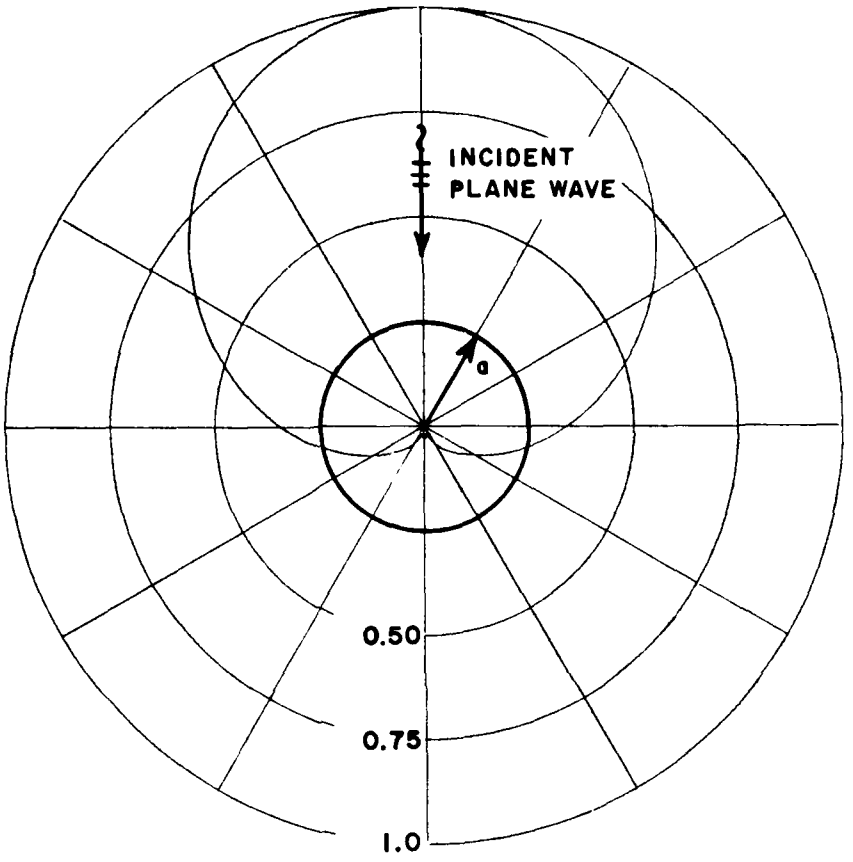

Figure 29. Isolated surface current density with plane wave incidence. (J^0) for geometry of Figure 27.

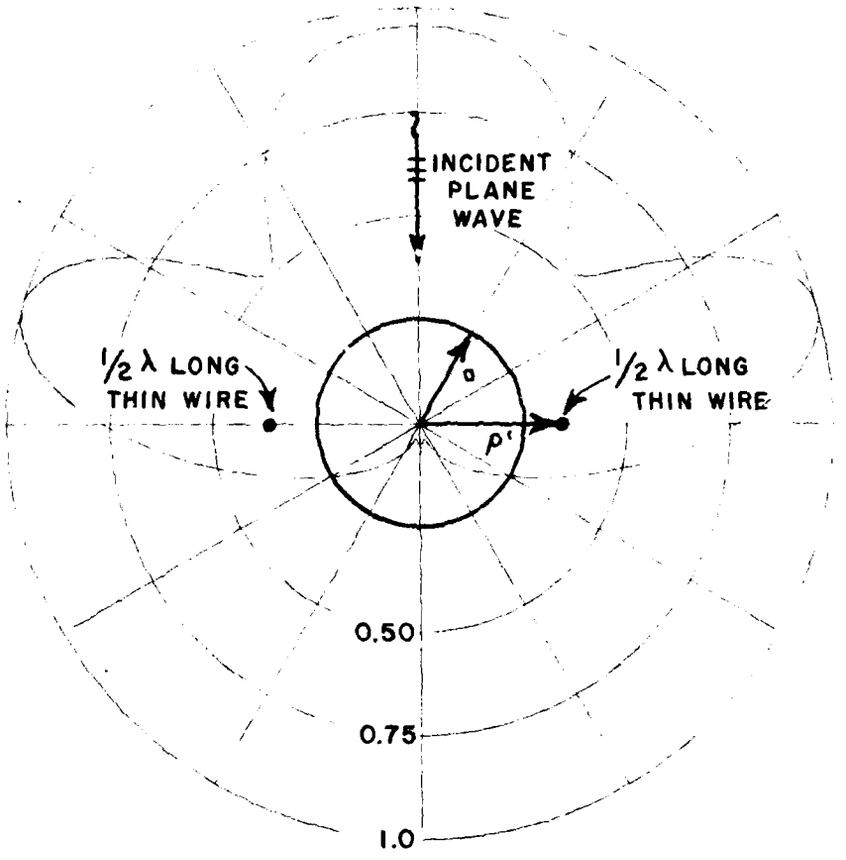

Figure 30. Normalized total surface current induced on an infinitely long circular cylinder with 1/2λ radius in the presence of two thin wires. Thin wires are located 1/2λ away from the cylinder. Scaling factor is 6.13 mAmp/meter.

SECTION V
FUSELAGE CURRENT DENSITIES FOR AIRCRAFT-LIKE STRUCTURE

As a next step, an aircraft-like structure is analyzed. A total of eighteen wires, nine on each side of the cylinder, is used in order to simulate the wings (0.3λ by 1λ long). The current distribution on these wires is obtained from the hybrid moment method solution as outlined previously. The geometry of this aircraft model is illustrated in Figure 31. The current density on the

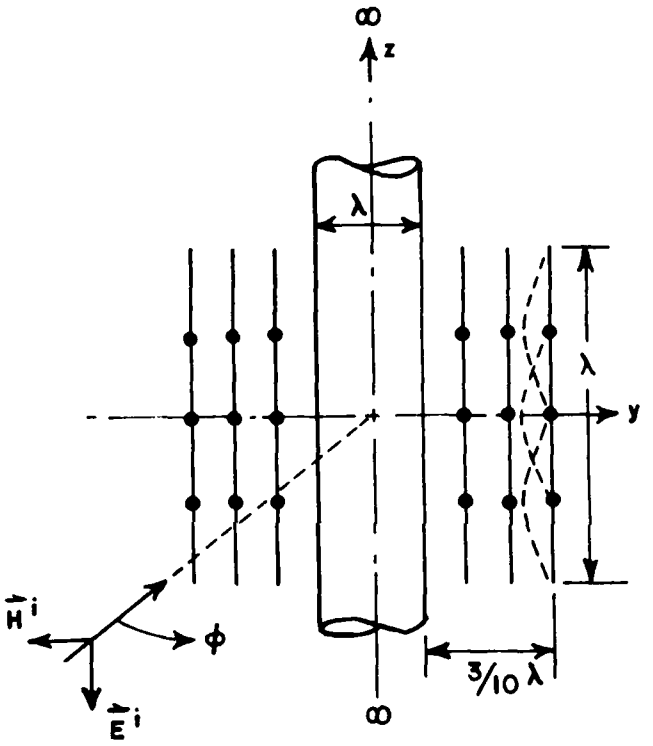

Figure 31. Aircraft geometry with 0.3λ by λ wings placed in a plane containing the cylinder axis.

cylinder as obtained from the hybrid moment technique is shown in Figure 32. In the same plot, a GTD solution is also presented [26]. Considering the limitation of the GTD solution for such a geometry, the results shown in Figure 32 are in reasonable agreement.

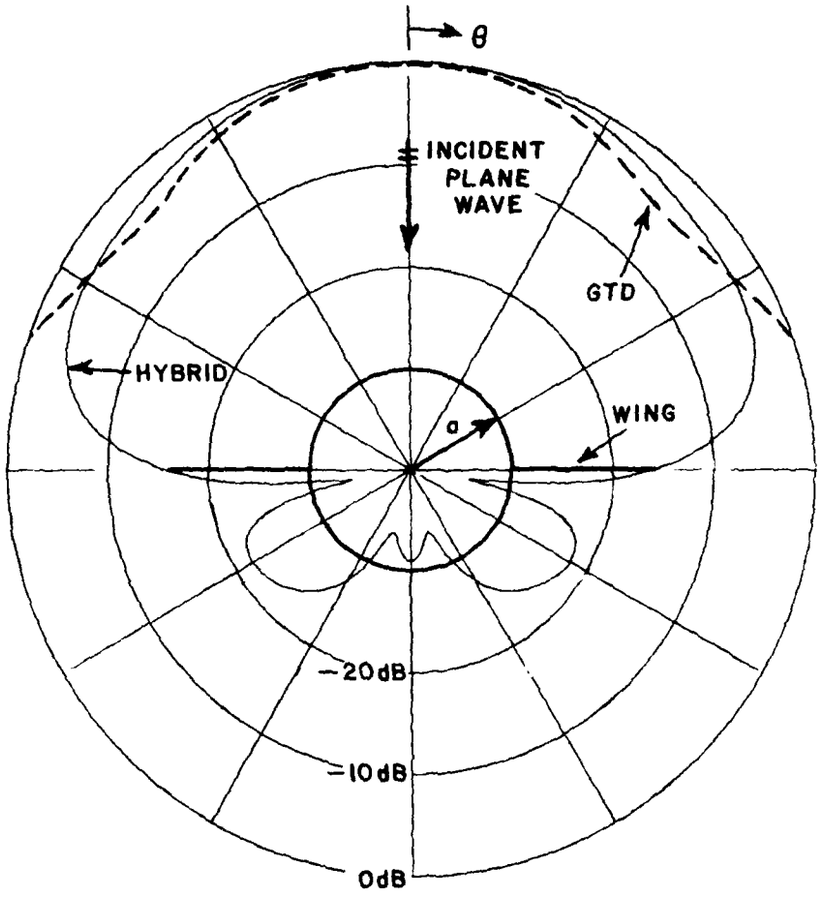

Figure 32. Surface current density induced on a fuselage as a function of ϕ angle for geometry of Figure 31.

An aircraft-like structure with one wavelength long square wings is also analyzed. Such an aircraft is presented in Figure 33. Both the field and the dB plots of the hybrid moment method results are included in Figures 34 and 35. In the same plots, related GTD solutions are shown as dotted lines. Again, up to the limitations of the GTD solution, the results are in reasonable agreement.

A linear plot of the surface induced current density on the fuselage and the wings for the same aircraft structure (Figure 33) is shown on Figure 36. The relationship $J_s=I_m/\Delta\ell$ is employed in order to obtain the surface current density on the wings. These results

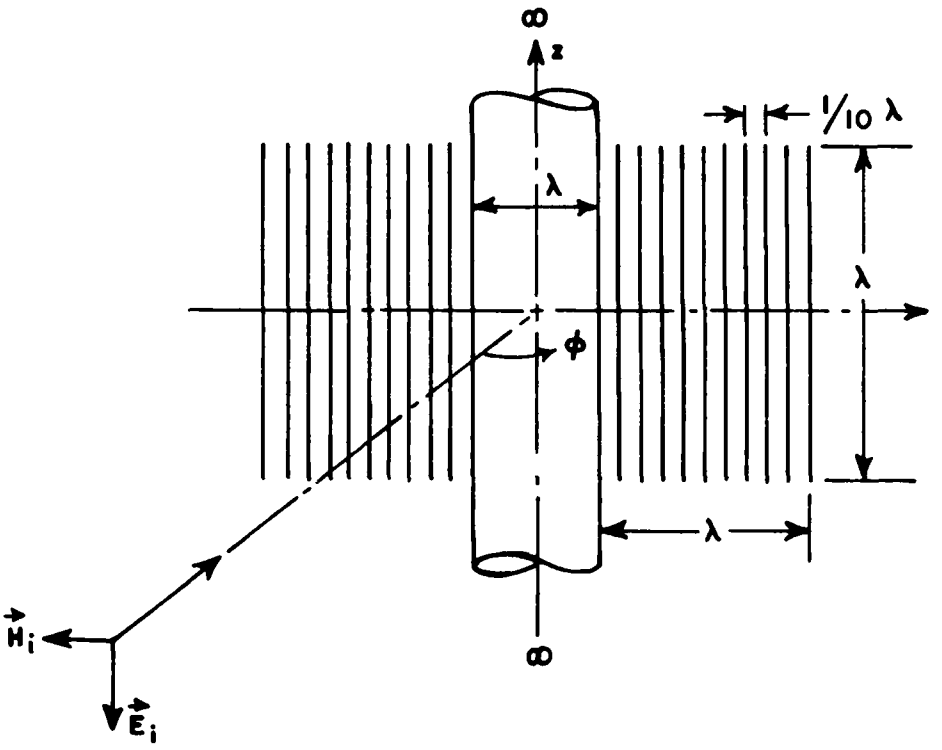

Figure 33. "Aircraft-like" geometry with 1λ by 1λ square wings placed on a plane containing the cylinder axis.

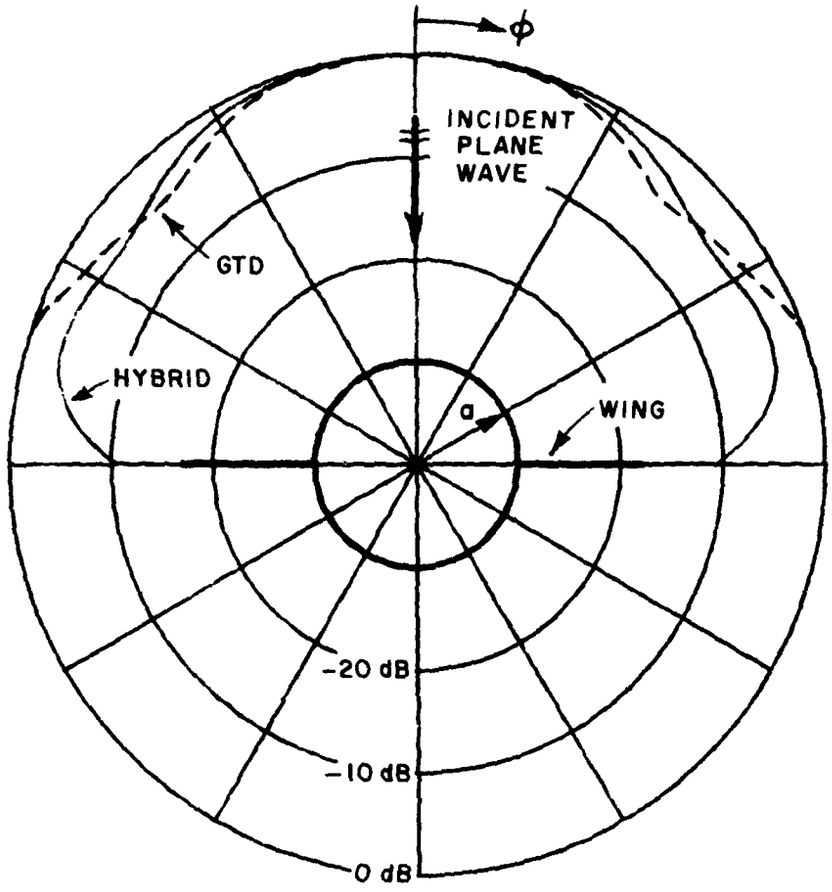

Figure 34. Surface current density induced on fuselage as a function of ϕ angle for geometry of Figure 33.

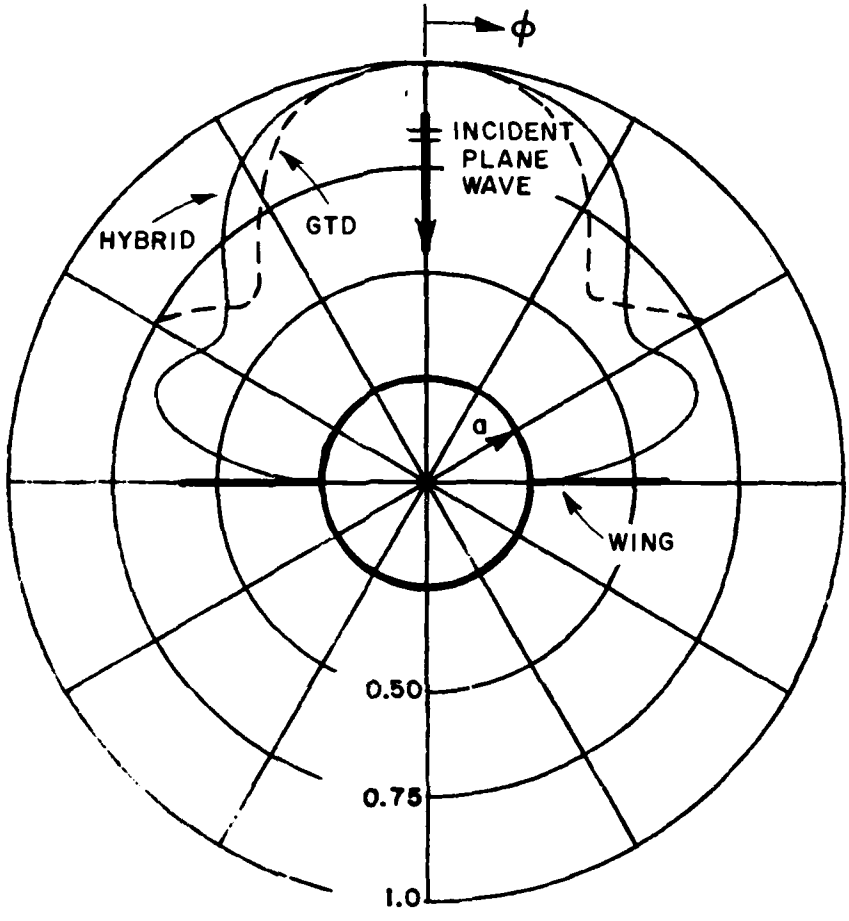

Figure 35. Surface current density induced on a fuselage as a function of ϕ angle for geometry of Figure 33.

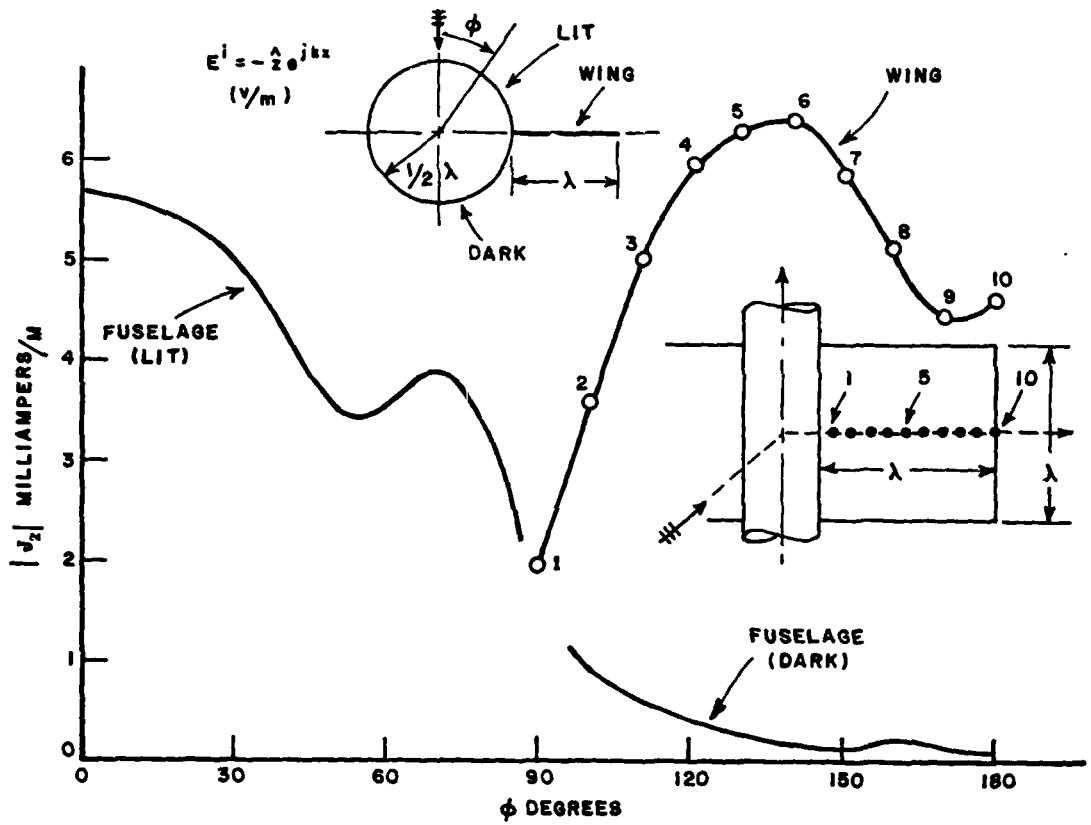

Figure 36. Current distribution induced on circular cylinder with thin wings by plane wave with normal incidence.

are compared with the results shown in Figure 37 obtained from two dimensional eigensolutions and a related moment method technique (strip model) where the wings are represented as infinitely long strips (patch type solution) and the fields are again expanded in terms of the cylindrical Green's functions [27]. The agreement between Figure 36 and Figure 37 is remarkable. Even the current density on the "wings" of the two structures is in good agreement. Only for the low level fields in the shadow region do these results show any significant difference.

Finally, the aircraft-like structure, shown in Figure 38, is analyzed. The purpose of this figure is to simulate a typical aircraft as closely as possible at a frequency where the GTD model is not valid. Total surface current density induced on the fuselage is shown in Figure 39. When Figure 39 is compared with the results obtained for isolated surface current density, $\overline{J}_s$ (i.e., without the wings), it is found that for this polarization, the wings shown in Figure 38 have almost no effect on the surface current density. In order to see how wide the wings should be before they can have a significant effect on the surface current distributions, isolated, perturbed and total surface current densities induced on a fuselage are plotted as a function of dipole length for a single dipole spaced $\lambda/10$ from the surface. These results are presented in Figure 40. As it can be seen from this figure the wings should be wider than 0.2λ before they can have any effect on the surface current density for this incidence and for this polarization.

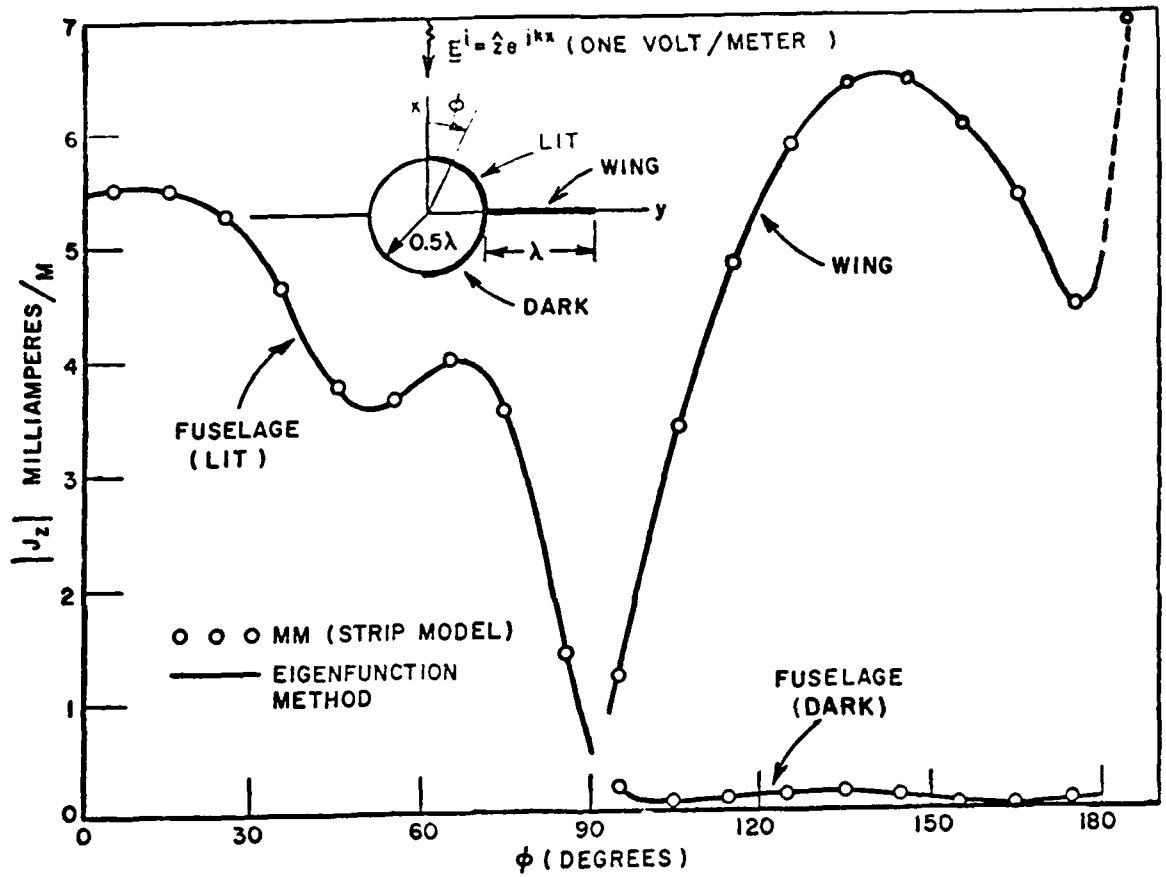

Figure 37. Current distribution induced on circular cylinder with thin wings by plane wave with normal incidence. (The cylindrical fuselage and wings have infinite length.) [27]

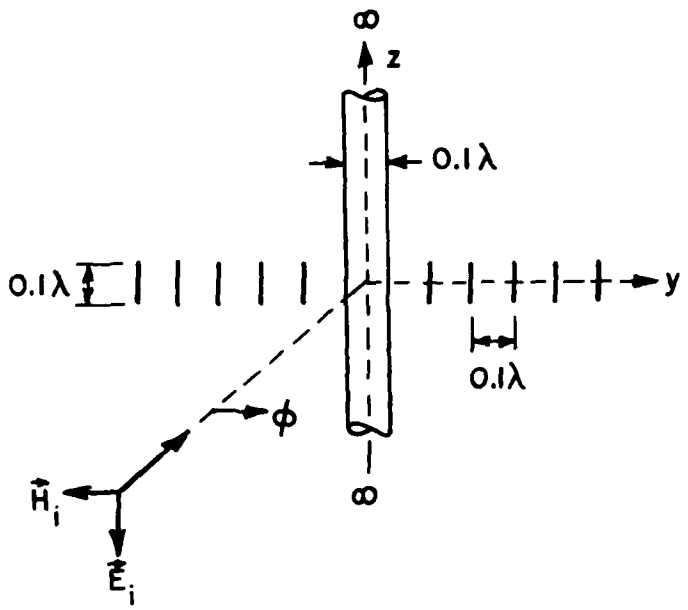

Figure 38. Aircraft-like structure with 0.1λ by 0.5λ wings placed on a plane containing the cylinder axis.

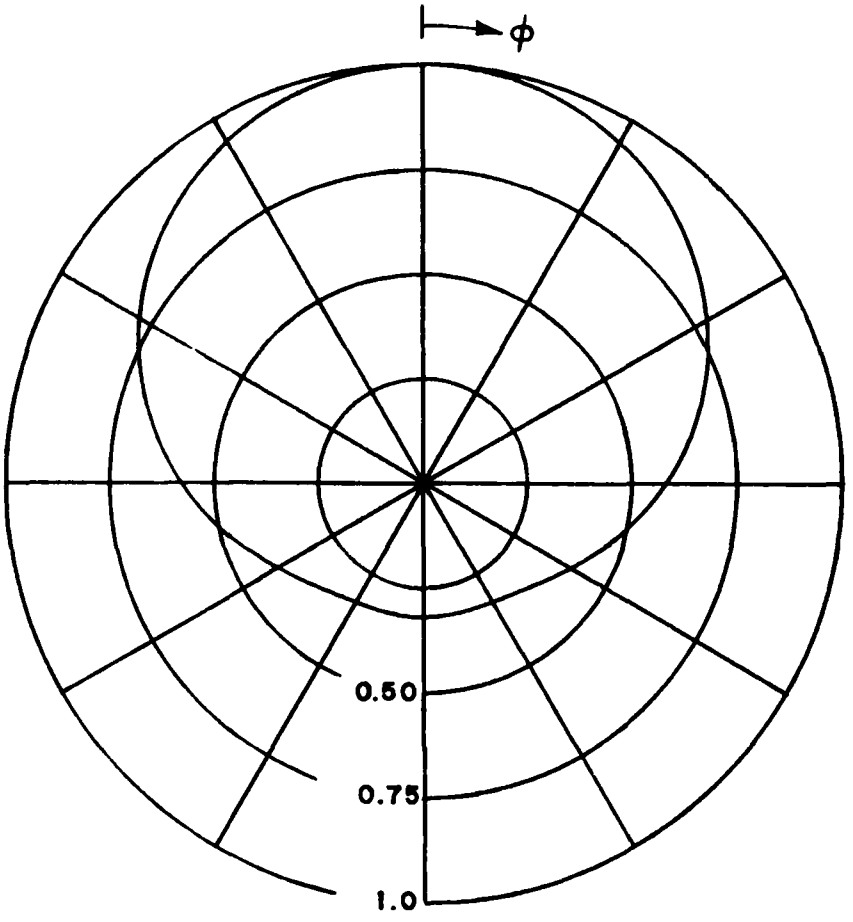

Figure 39. Surface current density on a fuselage as a function of ϕ angle for geometry of Figure 38.

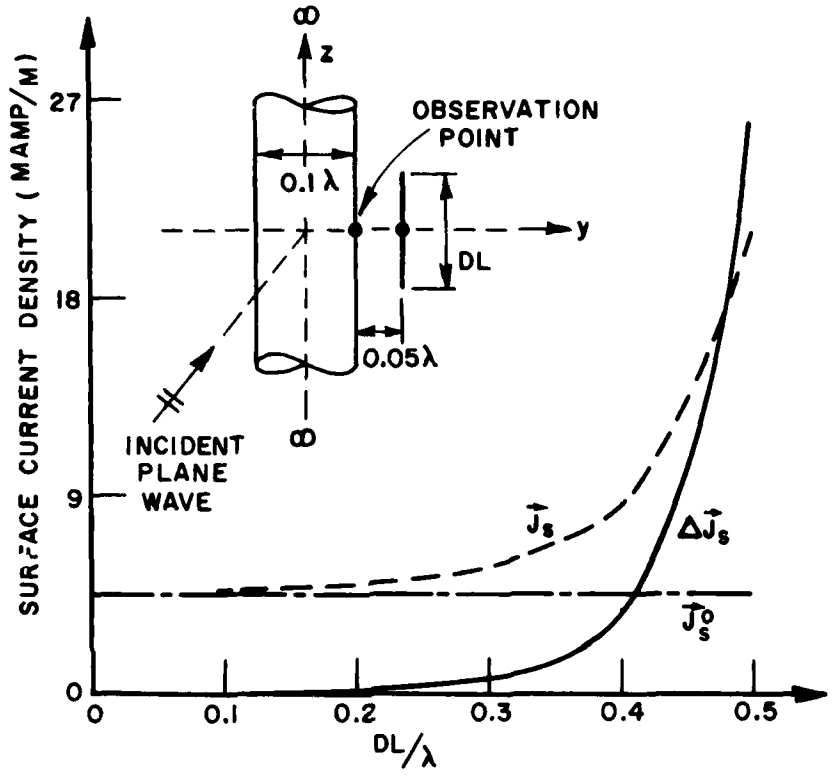

Figure 40. Total, perturbed and isolated surface current densities induced on an infinitely long circular cylinder as a function of dipole length.

SECTION VI
CONCLUSIONS AND RECOMMENDATIONS

The results obtained in this report show that the hybrid moment method solution outlined is a valid approach for calculating the induced surface current and charge densities on an infinitely long circular cylinder in the presence of axial thin wire segments. Rather simple aircraft models can be constructed by using such cylinders and axial dipoles when the geometry is selected carefully, and therefore the theory presented above can be used in the solutions of such structures. There remains the task of including the radial wires to make this solution more general. This has been partially completed to the extent that the cylindrical Green's functions $G_{\rho\rho}$ and the mutual impedances $Z_{\rho\rho}$ have been programmed. There remains in this solution to evaluate $G_{\rho\phi}$ and $Z_{\rho\phi}$ and then incorporate these quantities in the existing solution. If this solution is carried to completion, it will indeed help fill the void between the low frequency (moment method) and high frequency (GTD) solutions.

Some of these results can be used to infer a procedure for introducing the finite length of the fuselage itself at least for this particular type of aircraft and incidence plane. Figure 24 and Figure 25 show that the charge and current densities induced on the cylinders by the dipole are significant only a limited distance along the cylinder. These cases are for dipoles a distance of $\lambda/10$ away from the cylinder surface. As the dipoles are displaced a greater distance, these surface currents and charges would decay rather rapidly. Thus we observe that the currents on the dipoles representing the wings can be obtained rather accurately if only the fuselage in the vicinity of the wings can be represented by the infinite cylinder. Once these currents are known, they can then be used as sources (in addition to the plane wave excitation) exciting a finite length fuselage. Here, only the fuselage itself needs to be included in the impedance matrix. This means that a significantly larger aircraft could be modeled using moment method techniques.

As a final comment, once these mechanisms are all well established, a further substantial improvement can be obtained by introducing surface patches in place of the wire grid model. If all of these steps are carried to a proper conclusion then indeed this hybrid solution would fill the void that exists in the frequency domain between moment method and GTD solutions for surface current and charge densities that are excited by a plane wave incident on aircraft structures. It would then be possible to obtain realistic impulse response for these quantities and of course to find the response to any excitation in the time domain for these quantities.

REFERENCES

1. C. D. Taylor, K. T. Chen and T. T. Crow, "An Improvement on Wire Modeling for Determining the EMP Interaction With Aircraft: Applications to the B-1 Aircraft," Interaction Note 241, October 1974.

2. C. D. Taylor, K. T. Chen and T. T. Crow, "Electromagnetic Pulse Interaction with the EC-135 Aircraft," Interaction Application Memo 10, July 1975.

3. a) L. Peters, Jr., "High Frequency Surface Charge and Current Density Induced on the B-1 and 747 Aircrafts," Volume 1, Interaction Application Memo 7, January 1975.

   b) Y. Hwang, W. D. Burnside and L. Peters, Jr., "Early Time EMP Response of the Surface Current and Charge Densities on B-1 and 747 Aircrafts," Volume 2, Interaction Application Memo 7, January 1975.

4. P. R. Lentz, P. H. Pathak and W. D. Burnside, "Surface Current and Surface Charge Density Induced on Aircraft Models," Interaction Note 117, June 1972.

5. J. H. Richmond, "A Wire-Grid Model for Scattering by Conducting Bodies," IEEE Trans. Antennas and Propagation, Vol. AP-14, pp. 782-786, November 1966.

6. G. A. Richards, "A Boundary-Value Technique for Comparing the Patterns of an Antenna Near a Conducting Body of Arbitrary Shape," Report 2235-2, 11 September 1967, The Ohio State University ElectroScience Laboratory, Department of Electrical Engineering; prepared under Contract N00019-67-C-0063 for Naval Air Systems Command.

7. J. H. Richmond, "Computer Analysis of Three-Dimensional Wire Antennas," Report 2708-4, 22 December 1969, The Ohio State University ElectroScience Laboratory, Department of Electrical Engineering; prepared under Contract DAAD05-69-C-0031 for Ballistic Research Laboratory.

8. N. N. Wang, J. H. Richmond and M. C. Gilreath, "Sinusoidal Reaction Formulation for Radiation and Scattering from Conducting Surfaces," IEEE Trans. on Antennas and Propagation, Vol. AP-23, No. 3 (May 1975), pp. 376-382.

9. Y. T. Lin, "Classification of Objects with Complex Geometric Shape by Means of Low Frequency Electromagnetic Response," Report 3815-1, August 1974, The Ohio State University ElectroScience Laboratory, Department of Electrical Engineering; prepared under Grant AFOSR-74-2611 for Air Force Office of Scientific Research.

10. J. H. Richmond, (Private Communication).

11. Y. T. Lin and J. H. Richmond, "EM Modeling of Aircraft at Low Frequencies," IEEE Trans. Antennas and Propagation, Vol. AP-23, January 1975, pp. 53-56.

12. R. J. Marhefka, "Analysis of Aircraft Wing-Mounted Antenna Patterns," Report 2902-25, June 1976, The Ohio State University ElectroScience Laboratory, Department of Electrical Engineering; prepared under Contract NGL-36-008-138 for National Aeronautics and Space Administration.

13. W. D. Burnside, "Analysis of On-Aircraft Antenna Patterns," Report 3390-1, August 1972, The Ohio State University Electro-Science Laboratory, Department of Electrical Engineering; prepared under Contract N62269-72-C-0354 for Naval Air Development Center.

14. C. L. Yu and W. D. Burnside, "Volumetric Pattern Analysis of Fuselage-Mounted Airborne Antennas," Report 2902-24, April 1976, The Ohio State University ElectroScience Laboratory, Department of Electrical Engineering; prepared under Contract NGL-36-008-138, for National Aeronautics and Space Administration.

15. R. J. Marhefka, "Roll Plane Analysis of On-Aircraft Antennas," Report 3188-1, December 1971, The Ohio State University Electro-Science Laboratory, Department of Electrical Engineering; prepared under Contract N62269-71-C-0296 for Naval Air Development Center.

16. W. D. Burnside, M. C. Gilreath, R. J. Marhefka and C. L. Yu, "A Study of KC-135 Aircraft Antenna Patterns," IEEE Trans. Antennas and Propagation, Vol. AP-23, May 1975, pp. 309-316.

17. W. D. Burnside, R. J. Marhefka and C. L. Yu, "Roll-Plane Analysis of On-Aircraft Antennas," IEEE Trans. Antennas and Propagation, Vol. AP-21, November 1973, pp. 780-786.

18. J. B. Keller, "Geometrical Theory of Diffraction," Journal of the Optical Society of America, 52, Feburary 1962, pp. 116-130.

19. D. L. Hutchins and R. G. Kouyoumjian, "A New Asymptotic Solution to the Diffraction by a Wedge," URSI 1967 Spring Meeting, Ottawa, Canada, pp. 154-155.

20. P. K. Pathak and R. G. Kouyoumjian, "The Dyadic Diffraction Coefficient for a Perfectly-Conducting Wedge," Scientific Report No. 5, Report 2183-4, 5 June 1970, The Ohio State University ElectroScience Laboratory, Department of Electrical Engineering; prepared under Contract AF19(628)-5929 for Air Force Cambridge Research Laboratory.

21. R. G. Kouyoumjian, "Asymptotic High-Frequency Methods," Proceedings of the IEEE, Vol. 53, No. 8, August 1965, pp. 864-876.

22. J. H. Richmond, "Radiation and Scattering by Thin-Wire Structures in the Complex Frequency Domain," Interaction Note 202, May 1974.

23. R. F. Harrington, Field Computation by Moment Methods, The McMillan Company, N.Y., 1968.

24. R. F. Harrington, Time Harmonic Electromagnetic Fields, McGraw Hill Book Co., N.Y., 1961.

25. N. Wang, L. Ersoy and W. D. Burnside, "GTD Analysis and the Hybrid Techniques for the Investigation of the Surface Current and Charge Densities Induced on Aircraft," preliminary version of Interaction Note 338.

26. L. Ersoy, N. Wang, "User's Manual - The Surface Current Density and the Charge Density Induced on the Aircraft Fuselage for Arbitrary Plane Wave Incidence," Report 4172-1, July 1976, The Ohio State University ElectroScience Laboratory, Department of Electrical Engineering; prepared under Contract F29601-75-C-0086 for Air Force Contract Management Division.

27. N. Wang, (Private Communication).

28. J. J. Bowman, T. B. A. Senior and P. L. E. Uslenghi, Electromagnetic and Acoustic Scattering by Simple Shapes, North-Holland Publishing Company, Amsterdam, 1969.

29. M. Abramowitz and I. A. Stegur, Handbook of Mathematical Functions, Dover Publications, Inc., N.Y., 1970.

APPENDIX A
TE AND TM FIELDS SEPARABLE IN THE CYLINDRICAL COORDINATE SYSTEM

The harmonic electromagnetic fields listed below satisfy Maxwell's equations in a homogeneous source-free region [10].

TE Fields	TM Fields
$E_\rho = -C(j\omega\mu/\rho)\, R\, P'\, Z$	$E = C\, R'\, P\, Z'$
$E_\rho = C\, j\omega\mu\, R'\, P\, Z$	$E_\phi = C\,(1/\rho)\, R\, P'\, Z'$
$E_z = 0$	$E_z = C\,\beta^2\, R\, P\, Z$
$H_\rho = C\, R\, R'\, P\, Z'$	$H_\rho = C(j\omega\epsilon/\rho)\, R\, P'\, Z$
$H_\phi = C\,(1/\rho)\, R\, P'\, Z'$	$H_\phi = -j\omega\epsilon\, C\, R'\, P\, Z$
$H_z = C\,\beta^2\, R\, P\, Z$	$H_z = 0$

C denotes an arbitrary constant.

The time dependence $e^{j\omega t}$ is understood. R is a function of ρ only, P is a function of ϕ only, and Z is a function of z only. Primes indicate differentiation with respect to ρ, ϕ or z. The functions satisfy the following differential equations:

$$\rho \frac{d(\rho R')}{d\rho} + (\beta^2 \rho^2 - m^2) R = 0$$

$$P'' = -m^2 P$$

$$Z'' = -h^2 Z$$

where

$\beta^2 + h^2 = \omega^2 \mu\epsilon$, and β and h are constants.

Some solutions of these differential equations are listed below.

$R(\rho)$	$P(\phi)$	$Z(z)$
$J_m(\beta\rho)$	$\cos m\phi$	$\cos hz$
$N_m(\beta\rho)$	$\sin m\phi$	$\sin hz$
$H_m^{(1)}(\beta\rho)$	$e^{jm\phi}$	e^{jhz}
$H_m^{(2)}(\beta\rho)$	$e^{-jm\phi}$	e^{-jhz}

If $\beta = 0$, the radial function is $R(\rho) = \rho^{\pm m}$.

APPENDIX B
THE ELECTRIC DYADIC GREEN'S FUNCTION FOR THE CIRCULAR CYLINDER

The electric dyadic Green's functions for a circular cylinder with radius a is given as follows [28]

$$\tilde{\tilde{G}}_e(r|r_o) = \frac{-j}{8\pi}\int_{-\infty}^{\infty} dt \sum_{n=0}^{\infty} \frac{\varepsilon_n}{k^2-t^2}\Big\{M_{en}^{(3)}(t,r)[M_{on}^{(1)}(-t,r_o)+a_n M_{on}^{(3)}(-t,r_o)]$$

$$+ M_{on}^{(3)}(t,r)[M_{on}^{(1)}(-t,r_o)+a_n M_{on}^{(3)}(-t,r_o)]$$

$$+ N_{en}^{(3)}(t,r)[N_{en}^{(1)}(-t,r_o)+b_n N_{en}^{(3)}(-t,r_o)]$$

$$+ N_{on}^{(3)}(t,r)[N_{on}^{(1)}(-t,r_o)+b_n N_{on}^{(3)}(-t,r_o)]\Big\}, \quad \text{for} \quad \rho>\rho_o,$$

$$\tilde{\tilde{G}}_e(r|r_o) = \frac{-j}{8\pi}\int_{-\infty}^{\infty} dt \sum_{n=0}^{\infty} \frac{\varepsilon_n}{k^2-t^2}\Big\{[M_{en}^{(1)}(t,r)+a_n M_{en}^{(3)}(t,r)]M_{on}^{(3)}(-t,r_o)$$

$$+[M_{on}^{(1)}(t,r)+a_n M_{on}^{(3)}(t,r)]M_{on}^{(3)}(-t,r_o)$$

$$+[N_{en}^{(1)}(t,r)+b_n N_{en}^{(3)}(t,r)]N_{en}^{(3)}(-t,r_o)$$

$$+[N_{on}^{(1)}(t,r)+b_n N_{on}^{(3)}(t,r)]N_{on}^{(3)}(-t,r_o)\Big\}, \quad \text{for} \quad \rho<\rho_o,$$

with

$$a_n = -\frac{J_n'(a\sqrt{(k^2-t^2)})}{H_n^{(2)'}(a\sqrt{(k^2-t^2)})}, \quad b_n = -\frac{J_n(a\sqrt{(k^2-t^2)})}{H_n^{(2)}(a\sqrt{(k^2-t^2)})},$$

$$M_{e_o^n}^{(j)}(t,r) = e^{-j\pm z}\left[\mp \frac{n}{\rho} Z_n^{(j)}(\rho\sqrt{(k^2-t^2)}) \begin{matrix}\sin n\phi \\ \cos n\phi\end{matrix} \hat{\rho} - \frac{\partial Z_n^{(j)}(\rho\sqrt{(k^2-t^2)})}{\partial \rho} \begin{matrix}\cos n\phi \\ \sin n\phi\end{matrix} \hat{\phi}\right],$$

$$N_{e_o^n}^{(j)}(t,r) = \frac{1}{k} e^{-j\pm z}\left[-it \frac{\partial Z_n^{(j)}(\rho\sqrt{(k^2-t^2)})}{\partial \rho} \begin{matrix}\cos n\phi \\ \sin n\phi\end{matrix} \hat{\rho} \pm \frac{int}{\rho} Z_n^{(j)}(\rho\sqrt{k^2-t^2}) \begin{matrix}\sin n\phi \\ \cos n\phi\end{matrix} \hat{\phi}\right.$$

$$\left. + (k^2-t^2) Z_n^{(j)}(\rho\sqrt{(k^2-t^2)}) \begin{matrix}\cos n\phi \\ \sin n\phi\end{matrix} \hat{z}\right],$$

$j = 1,3$ and $Z_n^{(1)}(x) = J_n(x), Z_n^{(3)}(x) = H_n^{(2)}(x)$.

where $J_n(x)$ and $H_n^{(2)}(x)$ denote the cylindrical Bessel and Hankel functions.

Please be aware of the fact that in the above equations j is used in two different senses. In one case it denotes an integer, in the other case it means $\sqrt{-1}$. The time dependence $e^{j\omega t}$ is understood. For an arbitrarily oriented infinitesimal electric dipole located at $\bar{r}_o \equiv (\rho_o \geq a, \phi_o, z_o)$ with moment $(-j\omega\mu I d\ell)\hat{\ell}$, the total electric field is

$$\bar{E}^i(\bar{r}') + \bar{E}^s(\bar{r}) = -j\omega\mu I \, d\ell \, \tilde{\bar{G}}_e(r|r_o) \cdot \hat{\ell}$$

APPENDIX C

THE ELECTRIC DYADIC GREEN'S FUNCTION OF FREE SPACE

The electric dyadic Green's functions for free space [24]

$$G_{u_i u_i}(\bar{r}|\bar{r}_o) = \left(1 + \frac{1}{k^2}\,\frac{\partial^2}{\partial^2 u_i}\right)\psi$$

$$G_{u_i u_j}(\bar{r}|\bar{r}_o) = G_{u_j u_i}(\bar{r}\,\bar{r}_o) = \frac{1}{k^2}\,\frac{\partial^2}{\partial u_i \partial u_j}\psi \qquad i \neq j$$

where

$$u_i = x, y, z \quad \text{for} \quad i = 1,2,3$$

and

$$\psi = \frac{e^{-jk|\bar{r} - \bar{r}_o|}}{4\pi|\bar{r} - \bar{r}_o|} \quad .$$

APPENDIX D
LARGE ORDER APPROXIMATION FOR HANKEL FUNCTION

One of the difficulties encountered in this report is the numerical convergence problem. During this investigation, it is found that while the ratios of the cylindrical Bessel functions used for the calculations are not negligible, both the numerator and the denominator became very small for large orders when they are calculated individually. Because of the limitations of todays computers, when the ratio of two such small numbers is taken by the computer, it is set to zero even though it is very significant. This difficulty is overcome by calculating the ratio itself directly for large orders of Bessel functions. In this appendix, a suitable expression for this purpose is presented.

The ratio of two cylindrical Hankel functions with different arguments and large order is

$$\frac{H_n^{(2)}(n\rho')}{H_n^{(2)}(n\rho)} \approx \left(\frac{1-\rho^2}{1-\rho'^2}\right)^{1/4} \left\{\frac{\rho(1+\sqrt{1-\rho'^2})}{\rho'(1+\sqrt{1-\rho^2})} \exp\left[\sqrt{1-\rho^2}-\sqrt{1-\rho'^2}\right]\right\}^n$$

where n is the order [29]. The argument of the ratio can be complex. The relation between modified Hankel functions and regular Hankel functions can be used in order to obtain the ratio of modified Hankel functions such that

$$\frac{K_n(n\rho')}{K_n(n\rho)} = \frac{H^{(2)}(-jn\rho')}{H^{(2)}(-jn\rho)}$$

where $j = \sqrt{-1}$.


DA
FIL
3